The DOI for this manuscript is doi: 10.1175/BAMS-D-16-0215.1

The Arctic System Reanalysis Version 2

D. H. Bromwich[1,2], A. B. Wilson[1]*, L. Bai[1], Z. Liu[3], M. Barlage[4], C.-F. Shih[5], S. Maldonado[1,2], K. M. Hines[1], S.-H. Wang[1], J. Woollen[6], B. Kuo[7], H.-C. Lin[3], T.-K. Wee[8], M. C. Serreze[9], and J. E. Walsh[10]

[1] Polar Meteorology Group, Byrd Polar and Climate Research Center, The Ohio State University, Columbus Ohio, U.S.A.

[2] Atmospheric Sciences Program, Department of Geography, The Ohio State University, Columbus, Ohio, U.S.A.

[3] National Center for Atmospheric Research, Mesoscale and Microscale Meteorology Laboratory, Boulder, Colorado, U.S.A.

[4] National Center for Atmospheric Research, Research Applications Laboratory, Boulder, Colorado, U.S.A.

[5] National Center for Atmospheric Research, Computational Information Systems Laboratory, Boulder, Colorado, U.S.A.

[6] National Centers for Environmental Prediction, College Park, Maryland, U.S.A.

[7] University Corporation for Atmospheric Research, UCAR Community Programs, Boulder, Colorado, U.S.A.

[8] University Corporation for Atmospheric Research, Constellation Observing System for Meteorology, Ionosphere and Climate, Boulder, Colorado, U.S.A.

[9] National Snow and Ice Data Center, CIRES, University of Colorado – Boulder, Boulder Colorado, U.S.A

[10] International Arctic Research Center, University of Alaska – Fairbanks, Fairbanks, Alaska, U.S.A.

Submitted to the Bulletin of the American Meteorological Society
May 2017

Revised September 2017

+Contribution 1573 of the Byrd Polar and Climate Research Center

---

*Corresponding Author
Aaron B. Wilson
Byrd Polar and Climate Research Center
The Ohio State University
1090 Carmack Rd.
Columbus, Ohio 43210
Email: wilson.1010@osu.edu

ABSTRACT. The Arctic is a vital component of the global climate, and its rapid environmental evolution is an important element of climate change around the world. To detect and diagnose the changes occurring to the coupled Arctic climate system, a state-of-the-art synthesis for assessment and monitoring is imperative. This paper presents the Arctic System Reanalysis version 2 (ASRv2), a multi-agency, university-led retrospective analysis (reanalysis) of the Greater Arctic region using blends of the polar-optimized version of the Weather Research and Forecasting (Polar WRF) model and WRF three-dimensional variational data assimilated observations for a comprehensive integration of the regional climate of the Arctic for 2000-2012. New features in ASRv2 compared to version 1 (ASRv1) include 1) higher resolution depiction in space (15 km horizontal resolution), 2) updated model physics including sub-grid scale cloud fraction interaction with radiation, and 3) a dual outer loop routine for more accurate data assimilation. ASRv2 surface and pressure level products are available at 3-hourly and monthly-mean timescales at NCAR.

Analysis of ASRv2 reveals superior reproduction of near-surface and tropospheric variables. Broad-scale analysis of forecast precipitation and site-specific comparisons of downward radiative fluxes demonstrate significant improvement over ASRv1. The high-resolution topography and land surface, including weekly-updated vegetation and realistic sea-ice fraction, sea-ice thickness, and snow cover depth on sea ice, resolve fine-scale processes such as topographically-forced winds. Thus, ASRv2 permits a reconstruction of the rapid change in the Arctic since the beginning of the 21st century - complementing global reanalyses. ASRv2 products will be useful for environmental models, verification of regional processes, or siting of future observation networks.

CAPSULE. *The new regional-15 km Arctic System Reanalysis version 2 provides the accuracy and details necessary for many Arctic climate studies over the period 2000–2012.*

ARCTIC IN A STATE OF CHANGE. The Arctic is in the midst of rapid change in the physical environment with pronounced increases in surface air temperature, especially for winter and spring over subarctic land areas (Serreze and Francis 2006; Screen et al. 2012), as well as over the Arctic Ocean (e.g., Comiso 2003; Kohnemann et al. 2017). Arctic sea ice extent has declined throughout the satellite era, with the record September minimum extent in 2012 (Fig. 1) and the smallest maximum extent in March 2017 (NSIDC 2017). Sea-ice cover has thinned dramatically (Kwok and Untersteiner 2011), as historical evidence suggests that the recent seaice minima are unmatched across the Arctic back to 1850 (Walsh et al. 2017). Spring snow cover extents (SCE) over Eurasia and North America have significantly declined since 2005 (Arctic Report Card 2016), with Arctic SCE declining more rapidly than September minimum sea-ice extent (e.g., approximately -18% for June over the period 1967-2016; Derksen et al. 2017). Subsurface warming of the permafrost has also been observed in borehole measurements (e.g., Romanovsky et al. 2010). The area of the Greenland ice sheet experiencing summer melt has increased, and in mid July 2012 some 99% of the surface area was melting according to satellite observations, a highly unusual but not unique event (Nghiem et al. 2012). There has also been accelerated movement of Greenland outlet glaciers and increased runoff to the ocean (e.g., Rignot et al. 2011) as Greenland remains the largest land ice mass contributor to sea level rise (Harig and Simons 2016). However, glacier loss in other areas such as the Gulf of Alaska and the Canadian Archipelago are also significant contributors to sea level rise (Harig and Simons 2016) and may not be recoverable this century (Lenaerts et al. 2013). The symptoms of accelerated Arctic climate change are seemingly pervasive (IPCC 2013).

These changes may represent early signs of the expected Arctic amplification of the effects of increasing greenhouse gases (e.g., Screen and Simmonds 2010). However, the Arctic climate system is also home to strong natural variability (Kay et al. 2011; Ding et al. 2017), such as that associated with the North Atlantic Oscillation, the Arctic Oscillation, the Pacific Decadal Oscillation and other atmospheric patterns (Thompson and Wallace 2000; Rogers et al. 2001; Rigor and Wallace 2004; Hartmann and Wendler 2005; Overland and Wang 2005). Indeed, the increase in sea-ice volume in 2013 following the record minimum raises questions concerning the resilience of the Arctic sea-ice cover (Tilling et al. 2015). While there is some evidence that the signature of greenhouse has forcing has emerged in the Arctic over the last few decades (Fyfe et al. 2013), continued research to separate the forced response from intrinsic variability is needed. There is growing need to improve polar prediction and observing capacity, exemplified by the most recent polar endeavor, the Year of Polar Prediction (YOPP; Jung et al. 2016). This internationally coordinated effort of intensive observing and modeling activities will improve representation of polar processes in models and refine derived satellite products, among other benefits.

The community has long relied on global atmospheric reanalyses to explore climate system behavior. These syntheses merge a wide variety of surface, atmospheric and satellite remote sensing data into gridded analyses that are important resources for investigating Arctic climate change and accompanying variability during recent decades, most often since 1979 (e.g., Lindsay et al. 2014). There are nevertheless some important caveats to using global reanalyses for climate change assessment. While the use of a fixed data assimilation system and forecasting model eliminates spurious shifts in the output caused by model upgrades (e.g., Bengtsson and Shukla 1988), the reanalyses remain sensitive to changes in the observing system (e.g., Bengtsson et al. 2004a,b). For example, the European Centre for Medium-Range Weather Forecasts (ECMWF) interim reanalysis (ERA-Interim, hereafter ERAI; Dee et al. 2011) has artificial temporal trends due to the assimilation of rain-affected radiances from satellite passive microwave observations. The National Aeronautics and Space Administration Modern Era Retrospective-Analysis for Research and Applications (MERRA) (Rienecker et al. 2011) and the National Centers for Environmental Prediction (NCEP) Climate Forecast System Reanalysis (CFSR) (Saha et al. 2010) exhibit discontinuities associated with the start of the modern microwave sounder (ATOVS) era (Cullather and Bosilovich 2011; Zhang et al. 2012). Major temporal discontinuities have been largely resolved in MERRA version 2 (Gelaro et al. 2017). ERAI, MERRA, and CFSR showed significant errors in temperature, moisture, and wind speed in the lowest 800 m over the Arctic Ocean when compared to independent sounding observations (Jakobson et al. 2012).

The Arctic System Reanalysis (ASR) is a demonstration regional reanalysis for the greater Arctic (see Fig. 1) and an exercise well aligned with the goals of YOPP. ASRv2 spans the region poleward of the headwaters of the major rivers that flow northward into the Arctic Ocean and help maintain the low salinity of its near-surface layer. In Eurasia, these rivers are the Ob, Yenisei, Lena, and Kolyma while the Mackenzie is the largest such river in North America. Also the major oceanic storm tracks are included in the ASR domain. Particular attention has been paid to specifying realistic ocean and land surface conditions. Horizontal resolution is finer than the global reanalyses (35 km and coarser grids) and comparable time resolution is used. Optimal polar physics are used where possible. Currently, the period of assimilation is 2000-2012 that starts with launch of the NASA Earth Observing System satellite Terra (and later Aqua) that supplies several of the input data sets. As a result, ASR is particularly suitable for detailed investigations of near-surface characteristics during the period of rapid Arctic change, but lacks the multi-decadal perspective of the global reanalyses. Thus these different reanalyses are complementary to each other. ASR version 1 at 30 km grid spacing was outlined by Bromwich et al. (2016); the present manuscript describes ASR version 2 at 15 km grid spacing and illustrates its performance in relation to ASRv1 and ERAI.

PRODUCTION SYSTEM. ***Polar WRF.*** The regional forecast model used for ASRv2 is based on the Weather Research and Forecasting model (WRF) version 3.6.0 (Skamarock et al. 2008), utilizing the Advanced Research WRF (ARW) solver for fully compressible nonhydrostatic equations (Table 1). WRF has been optimized for polar environments (known as Polar WRF; http://polarmet.osu.edu/PWRF/) including improving the heat transfer through snow and ice (Hines and Bromwich 2008), the inclusion of fractional sea ice (Bromwich et al. 2009), the ability to specify variable sea-ice thickness, snow depth on sea ice, and sea-ice albedo (Hines et al. 2011, 2015; Wilson et al. 2011, 2012), and other optimizations included in the Noah Land Surface Model (LSM; Barlage et al. 2010). With the aid of the Mesoscale and Microscale Meteorology Division at NCAR, many of these routines developed by the Polar Meteorology Group of the Byrd Polar and Climate Research Center at The Ohio State University and are now part of the standard release of WRF (Powers et al. 2017; http://www.wrf-model.org/index.php).

The ASRv2 domain is the same as ASRv1 (Bromwich et al. 2016), consisting of a one-way nest, with an outer domain covering most of the Northern Hemisphere (NH) that provides smooth meteorological fields at the lateral boundaries of the inner domain (Fig. 1). The inner domain covers approximately 1.2 x 10^8 km^2 or about 50% of the NH. Care has been taken to avoid placing the inner domain boundaries across the highest topography ensuring a seamless transition of meteorological parameters. Polar WRF uses a staggered Arakawa grid-C with 721 x 721 grid points on a polar stereographic projection and 15 km horizontal resolution for the inner domain. In the vertical direction, Polar WRF uses a terrain-following dry hydrostatic-pressure coordinate system with 71 model levels and a constant pressure surface at the top of the model of 10 hPa. The lowest full model level is 4 m above ground level (AGL), with over 25 levels below 850 hPa, 0.5 km level spacing in the mid-troposphere, and approximately 0.8 km from the tropopause to the top of the model.

Initial and lateral boundary conditions for the outer domain in Polar WRF are provided by ERAI surface and upper air model-level data. To avoid model drift in atmospheric circulation (Glisan et al. 2013; Hines et al. 2015), spectral nudging is implemented on temperature, geopotential height and wind components above 100 hPa (top 20 vertical levels) on the inner domain (all levels in the outer domain). We use wavenumber 11 to impact only the large-scale synoptic conditions (wavelengths > 1000 km), and setting the nudging coefficients for all three variables to ten times the strength of ASRv1 removes additional upper-level model bias in the initial forecast. The top 8 km of Polar WRF are damped and the gravity wave drag option is selected to suppress gravity wave interference at the top of the model.

The physics parameterizations chosen for ASRv2 are based on extensive development and testing of Polar WRF over a wide-range of Arctic environments including the Greenland Ice Sheet and the Arctic Ocean (Hines and Bromwich 2008; Bromwich et al. 2009; Hines et al. 2011; Wilson et al. 2011, 2012; Hines et al. 2015). The Goddard microphysics scheme is utilized for the cloud microphysics with ice, snow, and graupel processes represented (Tao and Simpson, 1993; Tao et al., 2003). We use the Kain-Fritsch scheme (Kain and Fritsch, 1990, 1993; Kain, 2004) for the cumulus parametrization along with the climate model-ready update to the Rapid Radiative Transfer Model known as RRTMG for longwave and shortwave radiation (Clough et al. 2005; Iacono et al. 2008). Different from ASRv1 however, we implement the new subgrid-scale cloud fraction interaction with radiation that allows for more realistic shortwave and longwave, improving additional weather parameters (Alpaty et al. 2012; Zheng et al. 2016). The Noah Land Surface Model (LSM) (Chen and Dudhia, 2001), and the Mellor – Yamada – Nakanishi – Niino (MYNN) (Nakanishi, 2001; Nakanishi and Niino, 2004, 2006) 2.5 – level planetary boundary layer (PBL) and complementary surface layer schemes are also utilized.

WRF Data Assimilation (WRFDA) system overview. NCAR's community WRF data assimilation (WRFDA, formerly WRF-Var) system is adopted for the component of atmospheric analysis in the ASR project. Over recent years, WRFDA has been extended to include a broad range of data assimilation (DA) techniques, including 3DVAR, 4DVAR, and hybrid-EnVar approaches (Huang et al. 2009, Barker et al. 2012). ASR uses the 3DVAR technique that was more mature than other schemes (4DVAR and Hybrid-EnVar) in WRFDA at the time the project was originally proposed. WRFDA-3DVAR is based upon the MM5 3DVAR system (Barker et al. 2004), but the basic software framework are fully updated for the Advanced Research WRF model (ARW, Skamarock et al. 2008). It has been successfully implemented for operational/real-time applications at several numerical weather prediction centers and research institutes (Barker et al. 2012), including the Antarctic Mesoscale Prediction System (Powers et al. 2012).

WRFDA produces analyses of surface pressure and 3D atmospheric temperature, moisture and wind fields on the WRF model grid by assimilating many types of observations, including most conventional (both surface and upper air) and remote-retrieval observations as well as radiance data from a number of satellite platforms (Barker et al. 2012). [For a more detailed description of WRFDA see Skamarock et al. 2008.] All observations used in ASR are provided by the National Centers for Environmental Prediction (NCEP) in BUFR format. Figure 2 shows the typical coverage of non-radiance observations used in the ASR within a □1.5-hour data assimilation time window. High-latitude Arctic regions as well as ocean areas are sparsely monitored by conventional observations. Instead, non-radiance observations here are largely satellite atmospheric motion vectors and GPS radio occultation observations (assimilated as refractivity) providing upper air information along with surface ocean winds (at 10-m) from QuikScat.

SATELLITE RADIANCE ASSIMILATION. In addition to those non-radiance observations, radiance data from 12 microwave sensors (6 AMSU-A, 3 AMSU-B and 3 MHS) onboard 7 polarorbiting satellites, which have been proven to have a large positive impact on global medium-range forecast performance (e.g., Bouttier and Kelly 2001) and tropical storm forecasting using WRF (e.g., Liu et al. 2012, Schwartz et al. 2012), are also assimilated in ASR. Radiance observations are the major data source providing vertical temperature and moisture soundings over those regions with sparse conventional data coverage. For ASR, only the channels 5~9 (temperature sensitive) of AMSU-A and the channels 3~5 (moisture sensitive) of AMSU-B/MHS are used. High-peaking and surface-sensitive channels are not used because of the relatively low ASR model top (10 hPa) and inaccurate input of surface emissivity and skin temperature. Figure 3 depicts the time series over a period of 13 years (2000-2012) of global statistics of bias (left panels) and standard derivation (right panels) of observed minus calculated brightness temperatures using the Community Radiative Transfer Model (CRTM) (Han et al. 2006) with

ERAI as input, for AMSUA channels 5~9 and AMSU-B/MHS channels 3~5 respectively. These monitoring statistics were obtained using WRFDA's "offline" Variational Bias Correction (VarBC) option as described by Auligné et al. (2007) and Liu et al. (2012).

The starting dates from which radiance data become available are marked in Fig. 3 for the different instruments. The only sensor covering the whole ASR period is NOAA-15 AMSU-A. Monitoring statistics are a powerful tool for identification of bad channels within the lifetime of sensors, which have to be blacklisted in the data assimilation. For instance, METOP-2 AMSU-A channel 7 had a substantially increased standard deviation from January 2009 onward, which was known to suffer from increasing instrument noise and was turned off by operational data assimilation systems. The jump of both bias and standard deviation for NOAA-19 AMSU-A channel 8 can also be clearly seen from Fig. 3. Radiance blacklist table used in ASR is a combination of our monitoring results and blacklist tables used by NCEP operations (see http://www.emc.ncep.noaa.gov/mmb/data_processing/Satellite_Historical_Documentation.htm) and ERAI (Paul Poli, Personal Communication, 2012). Some important radiance blacklist decisions in ASR are marked in the right panel of Fig. 3. For instance, iuse (:) = -1 means all channels are turned off, and iuse(8) = -1 denotes that channel 8 is not used. It is evident that radiance bias characteristics of different channels have been evolving with time and exhibit to a different extent seasonal variations, posing the need for a time-evolving and adaptive bias correction scheme. A state-of-the-art VarBC scheme was implemented in WRFDA and used for ASR, which is similar to that used at NCEP (Derber and Wu, 1998) and ECMWF (Dee and Uppala, 2009). Offline monitoring statistics also provide pre-trained bias correction coefficients for individual channels, which are used as the initial condition of cycling VarBC scheme in different streams of ASR production runs and can minimize the spin-up effect of bias correction adjustment (Liu et al. 2012, Schwartz et al. 2012).

SURFACE OBSERVATION ASSIMILATION. WRFDA does not directly analyze the screenlevel atmospheric parameters (i.e., temperature/moisture at 2-m and wind at 10-m), which are important variables commonly used for climate trend analysis. Instead, WRFDA analyzes atmospheric variables at the lowest model level by assimilating 2-m temperature/moisture and 10m U/V wind observations from surface stations (SYNOP, METAR, SHIP, BUOY). The lowest model level of the ASR domain is at about 4 m, which allows 10-m wind analysis accurately derived from a vertical interpolation and 2-m T/Q analysis extrapolated using the model's local lapse rate. To account for the difference between model terrain and surface station elevation, terrain corrections are applied to surface observations (also including surface pressure) before they are assimilated. Note that 2-m temperature/moisture and 10-m U/V wind are the diagnostic, not prognostic variables in the WRF model. Therefore, their analyses do not affect the subsequent WRF model forecast during the ASR data assimilation/forecast cycles.

ATMOSPHERIC BACKGROUND ERROR COVARIANCES**.** Another important aspect is the background error covariance (BEC) statistics that constrain (together with observation errors) the weight between the model background (i.e., a 3-hr forecast from previous cycle's analysis) and the observations, and also propagate information from observed to unobserved areas/variables both in horizontal and vertical through spatial and multivariate correlations implied in the BEC. BECs for ASR were generated using the so-called "NMC" method (Parrish and Derber 1992), which takes differences between forecasts of different lengths valid at common times. ASR uses the differences of 24- minus 12-hr WRF forecasts, initialized from ERAI interpolated into the ASR grid and valid at either 0000 or 1200 UTC over different months.

LAND SURFACE. *Data Assimilation.* Land surface models coupled to mesoscale meteorological models have been shown to perform poorly at cold season processes, such as snowpack physics and soil heat diffusion, leading to an inadequate representation of spring snow melt timing and the soil temperature profile, two major metrics of climate change in the Arctic (Slater et al. 2007, Pan et al. 2003, Barlage et al. 2010). Addressing these model issues through data assimilation into land surface models is limited by the paucity of quality state variables at high latitudes. In the ASR, several existing global-scale satellite observations have been identified to improve the representation of the land surface. These data are either integrated directly into the model or used to develop new datasets consistent with the Noah land model infrastructure.

Currently in the WRF/Noah model, land surface properties, such as green vegetation fraction and albedo, are prescribed climatological values based on historical AVHRR satellite data. With the launch of the MODIS sensors on-board the NASA Terra and Aqua platforms in 1999 and 2002 and real-time vegetation monitoring by NOAA-NESDIS, the availability of high spatial and temporal resolution remotely-sensed land surface properties improved substantially. The primary concern in assimilating a wide variety of products is that they are consistent. For example, surface albedo is tightly coupled to snow cover so the system must consider this.

MODIS Albedo. The Noah land surface model treats albedo as a mixture of snow-free and snowcovered surface with the weighting based on model-diagnosed snow cover fraction. Satellite-based albedo observations are a combination of all surfaces present in the observation pixel. To use the satellite albedo within the Noah LSM, a disaggregation must be done, since the Noah LSM requires both a snow-covered and snow-free albedo regardless of the presence of snow. The Noah LSM also requires a snow-cover and snow-free albedo everywhere at all times, for example snowcovered albedo in the tropics.

Two new time-varying albedo datasets are created for snow-free and snow-covered surfaces using the MODIS 8-day 0.05° global albedo product (MODIS product code MCD43C3; Schaaf et al. 2002) along with the MODIS snow cover products (MOD10C2/MYD10C2; Hall et al. 2002). The MODIS data are first filtered using the albedo product quality flag and then using the snow product "cloud obscured" flag (data are rejected if cloud cover is greater than 80%). To determine the snow-covered albedo, the MODIS snow products must report at least 70% snow cover on the noncloud covered portion. Likewise, to be considered snow-free snow cover must be less than 10%. Since only one albedo observation is used to determine two necessary model inputs, a forward-intime and backward-in-time filling procedure is done using the nearest (in time) quality observation of either snow-covered or snow-free albedo for each global location. The resulting product for 2007 over a north Alaskan grid point (68.8°N, 154.9ºW) is shown in Fig. 4. These albedo products have been produced for 2000-2012.

Investigation of the above MODIS albedo (MCD43C3) over Greenland showed an unusual and unrealistic albedo time series. After analyzing a daily albedo dataset based on the MODIS daily snow cover product (MOD10A1/MYD10A1; Hall et al. 2002), the ASR albedo assimilation replaced the MCD43C3-based product with the MOD10A1-based product over the permanent ice portions of Greenland.

NOAA/NESDIS Green Vegetation Fraction. A real-time dataset of green vegetation fraction is produced weekly in near-realtime by NOAA/NESDIS (Jiang et al. 2008). This dataset is available for the entire ASR processing period at 0.144□ spatial resolution. This product is consistent with the current vegetation fraction data used in Noah. Therefore, no further parameter tuning is needed when using this product other than to reset maximum and minimum annual vegetation fraction range.

DATA ACCESS. ASRv2 data are available from the NCAR CISL Research Data Archive at https://rda.ucar.edu/datasets/ds631.1/.

EVALUATION. ***Surface.*** We compare near-surface variables from ASRv1, ASRv2, and ERAI to observations from ~5000 surface stations provided by the National Centers for Environmental Information (https://www.ncdc.noaa.gov/; counts vary by UTC hour, season, and year) and the Greenland Climate Network (GC-Net; http://cires1.colorado.edu/steffen/gcnet/) for the period January 2000 - December 2010 to compare the broad-scale performance of ASR at increasing horizontal resolution (Table 2; 80 km for ERAI to 15 km for ASRv2). All observed time series were screened for outliers and discontinuities. The results reflect reanalysis performance at 3-hr intervals in relation to surface observations that are mostly assimilated (except for GC-Net stations), and therefore are not entirely independent. Reanalysis values are spatially interpolated to the station locations from the surrounding 4 grid points. ASR is available every 3 hours while the ERAI is linearly interpolated between analysis times (00, 06, 12 and 18 UTC) to produce intermediate values (at 03, 09 UTC, etc.). Table values are 11-year averages for each month derived from averaging the results for all 5000 stations. Lower bias, smaller root mean square error (RMSE) and higher correlation show a better fit of the reanalysis to the observed time series. The 11-year mean is very similar to that obtained for each year.

Annual mean 10-m wind speed biases are smaller in the ASR products compared to ERAI, though a positive (negative) bias is demonstrated by ASRv2 (ASRv1). The annual spatial distribution of 10-m wind speed bias at the observation sites (Fig. 5) shows that ASRv2 almost everywhere has a reduced bias in comparison to ERAI, apart from Scandinavia, Europe, and the U.S. Midwest. Terrain variations not well resolved at 15 km (Fig. 1) may be partly responsible for the reanalysis challenges in Scandinavia and Europe. Table 2 reveals that there is a substantial improvement in RMSE and correlation between ERAI and ASRv2, where ASRv2 captures two-thirds of the 3hourly wind speed variance. Performance is better in summer than winter when the speeds are higher. As described in Bromwich et al. (2016), the improvements in near-surface wind are tied to the finer resolution in ASR and the improved skill in capturing local wind effects near complex terrain. ASRv1 (30 km) wind fields have been shown to be well represented, including wind related to topographically-forced wind events (Moore et al., 2016) and Arctic cyclones (Tilinina et al., 2014). The present results along with Moore et al. (2016) for ASRv2 demonstrate that local wind effects are even better captured by ASRv2 at 15 km resolution. (See Sidebar 1.)

Analysis reveals that ERAI and ASR products have small annual mean 2-m temperature biases, with the smallest biases represented by ASRv2. However, ASRv2 is colder than both ASRv1 and ERAI with small negative biases from January through October. However, these biases are well within the statistical error inherent in the model version change between ASRv1 and ASRv2. The annual spatial bias (Fig. 5) confirms the bias magnitude reduction in ASRv2 in comparison to ERAI except in the same problematic areas as for wind speed (Scandinavia, Europe, and U.S. Midwest). Nearly halving of the annual mean RMSE value from ERAI to ASRv2 (Table 2) indicates that ASRv2 shows a much closer fit to the observations and the standard deviation of unexplained variance is small. This is further supported by increasing skill indicated by higher correlation.

Annual mean 2-m dew point biases are similar between the reanalyses. Negative monthly dew point biases but small positive 2-m temperature biases for ASRv1 from April through October indicate drier than observed conditions. Negative 2-m temperature biases but positive dew point biases during the summer months in ASRv2 reflect ample moisture due to the improved cloud processes implemented in ASRv2. Again, lower annual mean RMSE and higher correlation in ASRv2 show an improvement in overall fit and skill.

All three reanalyses capture the surface pressure (atmospheric circulation) very well with very small biases, low RMSEs, and very high correlations. Consistent with other near-surface variables, the RMSE decreases from ERAI to ASRv2. To summarize, ASRv2 at 15 km shows a close fit to the surface observations throughout the year with the "large-scale parameter" surface pressure being the most skillful and the "more localized parameter" surface wind speed being less so.

Upper Air. For analysis of the upper air variables in ASRv2, we have selected 500 hPa temperature and 700 hPa relative humidity for comparison with ERAI for the period December 2006 –

November 2007 (Fig. 6). Figure 6a shows the annual mean 500 hPa temperature in ASRv2. The pattern aligns closely with the expected mean large-scale circulation. The coldest temperatures are located in the vicinity of the largest troughs, centered over Canada (~75°W) and Siberia (~140°E). A weaker trough is indicated over eastern Europe (~45°E) as well, with the strongest gradients throughout the mid-latitudes within the major troughs. Figure 6b shows the differences between ASRv2 and ERAI, which are generally within ±0.1°C. This is similar to the radiosonde comparison conducted by Bromwich et al. (2016) for ASRv1 and ERAI. The differences do not reveal systematic biases with scattered differences likely tied to small local variations between the reanalyses' assimilations. The greatest differences occur throughout the North Pacific, North Atlantic, and in areas of complex terrain.

Relative humidity at 700 hPa illustrates the middle troposphere (~3000 m), which is the level at which most weather systems are steered across the NH. Figure 6a depicts the annual mean relative humidity for December 2006-November 2007 showing a general low-to-high latitude gradient. The lowest relative humidity is found in the arid desert regions of the U.S. southwest (30-35°N, 110-125°W) and Middle East (30°N, 50°E) and near the influence of subtropical high in the Pacific. Higher relative humidity north of 40°N is associated with the major NH storm tracks and cooler cloudier environments. The onshore flow along the west coast of North America (55-65°N, 115-165°W) is highlighted by the higher relative humidity in this location, along with areas in SW Greenland (60-65°N, 30-45°W), western Scandinavia (60-70°N, 5-40°E), and across Siberia (5570°N, 75-165°E). An area of slightly lower relative humidity is located in vicinity of the Beaufort Sea High (70-80°N, 110-180°W), which was exceptionally strong during this period and has been linked number of teleconnections and summer sea-ice decline (L'Heureux et al. 2008;

Serreze and Barrett 2011). Figure 6d shows the differences between ASRv2 and ERAI, where magnitudes are generally within ±4%. ASRv2 has higher relative humidity across the main oceanic storm track regions of the North Pacific and Atlantic, and smaller positive differences compared to ERAI across much of the Arctic. ASRv2 demonstrates lower relative humidity across much of the continental areas of Eurasia. Compared to the analysis with radisondes (Bromwich et al. 2016), these results are comparable to an average 2% deficit in the RH across the domain with slightly higher RH in ASRv2 than ERAI.

Precipitation. We compare ASRv2 mean annual total forecast precipitation to ERAI for the 20002010 period (Fig. 7). ASRv2 mean precipitation (Fig. 7a) clearly depicts the major storm tracks of the North Pacific and Atlantic where over 2000 mm of annual precipitation falls. Greater amounts are also shown along the higher terrain of western North America. Much lighter amounts (< 600 mmm) fall across much of the Arctic Basin and in the desert regions of the Mideast. Figure 7b shows that differences between ASRv2 and ERAI across much of the domain are generally ±10%. Both storm track regions show up to 10% less annual precipitation in ASRv2 than in ERAI. The greatest difference between the two reanalyses occur over the highest terrain in western North America, the higher elevations throughout central Asia, and Greenland where difference are in excess of 50%. Across much of the Arctic, differences are small; though ASRv2 is dry (~15%) relative to ERAI throughout much of the western Arctic Basin.

To evaluate monthly and seasonal characteristics of precipitation in ASRv2 and improvements over ASRv1, we repeat our analysis from Bromwich et al. (2016; ASRv1 included here for comparison) for the period December 2006 – November 2007 using the Global Historical Climate

Network version 2 (GHCN2) (Peterson and Vose, 1997) and the Adjusted Historical Canadian Climate Data (AHCCD) (Mekis and Hogg, 1999) precipitation gauges (Fig. 7a). Each have undergone quality control procedures to improve wind under catch, evaporation and adjustments for trace observations, all particularly important for Arctic precipitation (Peterson and Easterling, 1994; Easterling and Peterson, 1995; Mekis and Hopkinson, 2004; Mekis, 2005; Devine and Mekis, 2008). We only used stations with complete annual records and divide the analysis between midlatitude (south of 60°N – 296 stations) and polar (north of 60°N – 78 stations).

Compared to the mid-latitude stations (Fig. 7c), we note further improvements in the summertime precipitation for this particular season (summer 2007). Monthly biases for April-July are smaller in ASRv2 than in ASRv1 (10-15%), though still generally over predicted and higher than those demonstrated by ERAI. While warm season precipitation is well captured by ASRv2, the cooler season shows drier biases in ASRv2 from August through March. For the polar stations (Fig. 7d), ASRv2 is comparable to ERAI from March through October. Significant improvements of over ASRv1 (> 10%) occur during the warmer months of May-August. Similar to the mid-latitudes however, November through February are generally drier in ASRv2 than in ASRv1 or ERAI.

Downward Radiation at the Surface. Annual mean incident shortwave (SW) and downwelling longwave (LW) from the Earth's Radiant Energy System, Energy Balance and Filled (CERESEBAF; Loeb et al. 2009, Kato et al. 2013) monthly 1° x 1° dataset are compared to ASRv2 and ERAI for December 2006 – November 2007 (Fig. 8). These data were obtained from the NASA Langley Research Center CERES ordering tool at (http://ceres.larc.nasa.gov/). CERES-EBAF has shown greater accuracy compared to other gridded radiation products as it incorporates detailed cloud and aerosol information (Ma et al. 2015; Wild et al. 2013, 2015; Zhang et al. 2015, 2016). Figure 8 also depicts additional ground-based measurements from independent sites (black dots; Abisko, Sweden; Atqasuk, Alaska U.S.A.; Sondankyla, Finland; and Summit, Greenland) and others that are part of the World Climate Research Program Baseline Surface Radiation Network (BSRN; Hegner et al. 1998; Ohmura et al. 1998). These stations provide a validation of CERESEBAF and a comparison between ERAI, ASRv1 (Bromwich et al. 2016), and ASRv2 (Table 3).

[For a full description of the radiation data, see Wilson et al. 2012)].

Figure 8a shows ASRv2 SW compared to the CERES-EBAF surface product. In general, ASRv2 has too much incident SW at the surface across much of the domain, with differences of 20-50 W m^{-2}. Small negative biases (0 to -20 W m^{-2}) are located over the western Arctic Ocean, Hudson Bay, and some parts of Baffin Bay. Conversely, ERAI has generally too much SW compared to the CERES-EBAF over the mid-latitudes (Fig. 8b), but too little across the central Arctic where differences exceed 20 W m^{-2}. Comparing these locations to Table 3, differences are consistent between CERES-EBAF and comparisons made at ground-stations. For SW, both ASRv2 and ERAI show an excess of SW, with the greatest differences occurring during the summer months. Though ASRv2 SW biases are greater than ERAI, they are much improved over ASRv1 with a decrease from annual mean bias of 42 W m^{-2} to 27 W m^{-2} in the mid-latitudes. Likewise, RMSE is lower (95.3 W m^{-2}) and correlations are greater (0.92) than ERAI. Table 3 also supports the findings demonstrated by Figs. 8a-b for the polar stations, with too much shortwave in ASRv2 (annual mean bias of 14.8 W m^{-2}) and too little in ERAI (annual mean bias of -6.7 W m^{-2}).

Figure 8c shows that ASRv2 generally predicts too little LW radiation across the domain, with differences between CERES-EBAF in the Arctic region of -10 to -20 W m^{-2}. Coupled with Fig. 8a, and despite the improved model cloud physics in Polar WRF, these biases indicate that additional model improvements are necessary in order to fully capture the radiative cloud effects. Comparatively, ERAI produces too much LW over the Arctic Ocean with differences of up to 20 W m^{-2} (Fig. 8d) indicative of too much cloud cover or optically thick clouds in that region.

Comparing these spatial plots to Table 3, again we see consistency as the stations indicate negative LW biases throughout the mid-latitudes. ASRv2 improves over both ASRv1 (-11.4 W m^{-2}) and ERAI (-8.8 W m^{-2}) with a mean annual bias of -6.8 W m^{-2}. Unlike the SW, similar negative LW biases occur throughout the year for both ASRv2 and ERAI. In the polar region, consistently low LW biases are evident throughout the annual cycle, and the LW bias in ASRv2 is slightly degraded (-13.9 W m^{-2}) compared to ASRv1 (-11.8 W m^{-2}). Ultimately, these results reflect strongly on analysis by Hines and Bromwich (2017), who demonstrate that in order to accurately predict Arctic low-clouds, models need accurate cloud condensation nuclei predictions.

CONCLUSIONS. In this paper we have described ASRv2, a new high-resolution regional reanalysis of the Greater Arctic covering the period from January 2000 to December 2012. This paper details the production system for ASRv2, including the Polar WRF specifications, WRFDA data assimilation routine, and observational datasets. Noted enhancements over ASRv1 (Bromwich et al. 2016) include increasing the horizontal resolution to 15 km, upgrading Polar WRF and cloud physics, adding a dual outer loop routine in the data assimilation to ensure a better fit between the model first guess and observations at analysis time, and additional nudging in the upper levels to remove model biases.

The surface and upper air analysis fields and forecast precipitation and downward radiation at the surface have been analyzed. Surface analysis with approximately 5000 surface stations reveals superior comparison in ASRv2, particularly driving down the 10-m wind speed biases and significantly improving the correlations over ASRv1 and ERAI. The upper-air analysis shows an extremely close comparison between ASRv2 and ERAI in 500 hPa temperature and 700 hPa relative humidity, with differences generally within ±0.1°C and ±4%, respectively. Precipitation analysis shows that we have markedly improved summertime precipitation, decreasing the biases during this season by 10-15%, but a dry bias remains during the cool months. Though comparison between downward radiation at the surface and satellite-derived values reveal that ASRv2 still produces too much shortwave and too little longwave in the forecasts, biases for these values in the mid-latitudes are nearly half compared to ASRv1 and the improvement is attributed to the inclusion of sub-grid scale cloud fraction interaction with radiation. Thus, ASRv2 has been shown to be an important synthesis tool for the detection and monitoring of Arctic climate change. (See Sidebar 2.) ASRv2 provides important benefits to the research community, in particular those in need of atmospheric data to conduct process studies of Arctic phenomena (e.g., local transport, fluxes, etc.) and to drive other environmental models.

Looking forward, of immediate concern is updating ASRv2 beyond 2012 to the present. It is important to continue to capture the accelerated climate changes taking place in the Arctic. This includes declining sea-ice and snow cover across the Arctic, variables that are likely to be better observed through satellite platforms such as Cryosat2 and ICESat-2. Likewise, there is growing support within the Arctic community for an extension of ASR back to 1979 with refinements to the atmosphere, land surface, sea-ice modeling, and data assimilation. This will provide a longer context from which to compare the most rapidly changing period in the Arctic to changes that occurred prior to 2000.

ACKNOWLEDGMENTS. This work was supported by the National Science Foundation (NSF) through grants ARC-0733023 and ARC-1144117 and by the National Aeronautics and Space Administration (NASA) grant NNX12AI29G. The authors thank the Ohio Supercomputer Center (http://www.osc.edu) for their use of the Oakley, Ruby, and Owens Clusters in order to conduct ASRv2. The authors would also like to acknowledge the early work conducted by the late Andrew Slater on this project, and thank the anonymous reviewers for their feedback and suggestions.

REFERENCES

Alapaty, K., J. A. Herwehe, T. L. Otte, C. G. Nolte, O. R. Bullock, M. S. Mallard, J. S. Kain, and J. Dudhia, 2012: Introducing subgrid-scale cloud feedbacks to radiation for regional meteorological and climate modeling. *Geophys. Res. Lett.*, **39**, L24809, doi:10.1029/2012GL054031.

Arctic Report Card, 2016: Accessed 4/27/2017. [Available online at http://arctic.noaa.gov/Report-Card.]

Auligné, T., A. P. McNally, and D. P. Dee, 2007: Adaptive bias correction for satellite data in a numerical weather prediction system, *Q. J. R. Meteorol. Soc.,* **133**, 631–642.

Bamber J. L., S. Ekholm, and W. B. Krabill, 2001: A new, high-resolution digital elevation model of Greenland fully validated with airborne laser altimeter data. *J. Geophys. Res.* **106**, B4, 6733 – 6745.

Barker D. M., W. Huang, Y.-R. Guo, A. J. Bourgeois, and Q. N. Xiao, 2004: A three-dimensional (3DVAR) data assimilation system for use with MM5: Implementation and initial results. *Mon. Wea. Rev.*, **132**, 897 – 914.

——, and Coauthors, 2012: The Weather Research and Forecasting Model's Community Variational/Ensemble Data Assimilation System: WRFDA. *Bull. Amer. Meteor. Soc.*, **93**, 831–843.

Barlage, M., and Coauthors, 2010: Noah land model modifications to improve snowpack prediction in the Colorado Rocky Mountains. *J. Geophys. Res.*, **115**, D22101, doi:10.1029/2009JD013470.

Bengtsson, L., and J. Shukla, 1988: Integration of space and in situ observations to study global climate change. *Bull. Amer. Meteor. Soc.*, **69**, 1130–1143.

——, S. Hagemann, and K. I. Hodges, 2004a: Can climate trends be calculated from reanalysis data? *J. Geophys. Res.*, **109**, D11111, doi: 10.1029/2004JD004536.

——, K. I. Hodges, and S. Hagemann, 2004b: Sensitivity of the ERA-40 reanalysis to the observing system: Determination of the global atmospheric circulation from reduced observations. *Tellus*, **56A**, 456–471.

Bouttier F. and G. Kelly, 2001: Observing-system experiments in the ECMWF 4D-Var data assimilation system, *Q. J. R. Meteorol. Soc.*, **127**, 1469-1488.

Bromwich, D. H., K. M. Hines, and L.-S. Bai, 2009: Development and testing of Polar WRF: 2. Arctic Ocean. *J. Geophys. Res.*, **114**, D08122, doi:10.1029/2008JD010300.

——, A. B. Wilson, L. Bai, G. W. K. Moore, and P. Bauer, 2016: A comparison of the regional Arctic System Reanalysis and the global ERA-Interim Reanalysis for the Arctic. *Q. J. R. Meteorol. Soc.*, **142**, 644-658, doi: 10.1002/qj.2527.

Chen F., and J. Dudhia, 2001: Coupling an advanced land surface-hydrology model with the Penn State-NCAR MM5 modeling system. Part I. Model and implementation and sensitivity. *Mon. Wea. Rev.*, **129**, 569 – 585.

Clough, S. A., M. W. Shephard, E. J. Mlawer, J. S. Delamere, M. J. Iacono, K. Cady-Pereira, S. Boukabara, and P. D. Brown, 2005: Atmospheric radiative transfer modeling: A summary of the AER codes. *J. Quant. Spectrosc. Radiat. Transfer*, **91**, 233–244, doi:10.1016/j.jqsrt.2004.05.058.

Comiso, J., 2003: Warming trends in the Arctic from clear-sky satellite observations. *J. Climate*, **16**, 3498-3510, doi: 10.1175/1520-0442(2003)016<3498:WTITAF>2.0.CO;2.

Cullather, R. I., and M. G. Bosilovich, 2011: The moisture budget of the polar atmosphere in MERRA. *J. Climate*, **24**, 2861–2879.

Dee, D. P., and S. M. Uppala, 2009: Variational bias correction of satellite radiance data in the ERA-Interim reanalysis. *Quart. J. Roy. Meteor. Soc.*, **135**, 1830–1841.

——, and Coauthors, 2011: The ERA-Interim Reanalysis: Configuration and performance of the data assimilation system. *Q. J. R. Meteorol. Soc.*, **37**, 553 – 597, doi:10.1002/qj.828.

Derber, J. C., and W.-S. Wu, 1998: The use of TOVS cloud-cleared radiances in the NCEP SSI analysis system. *Mon. Wea. Rev.*, **126**, 2287–2299.

Derksen, C., R. Brown, L. Mudryk, and K. Luojus, 2017: Terrestrial snow cover [in "State of the Climate in 2016"]. *Bull. Amer. Meteor. Soc.,* ***98*** *(8), S93–S98, doi:10.1175/2017BAMSStateoftheClimate.1.*

Devine K. A., and È. Mekis, 2008: Field accuracy of Canadian rain measurements. *Atmos. Ocean*, **46**, 213-227.

Ding, Q., and Coauthors, 2017: Influence of high-latitude atmospheric circulation changes on summertime Arctic sea ice. *Nature Climate Change*, **7**, 289–295, doi: 10.1038/nclimate3241.

Easterling D. R., and T. C. Peterson, 1995: A new method for detecting undocumented discontinuities in climatological time series. *Int. J. Climatol.*, **15**, 369-377.

Fyfe, J. C., K. von Salzen, N. P. Gillett, V. K. Arora, G. Flato, and J. R. McConnell, 2013: One hundred years of Arctic surface temperature variation due to anthropogenic influence. *Nature Sci. Rep.,* **3**, 2645, doi:10.1038/srep02645.

Gelaro, R., and Coauthors, 2017: The Modern-Era Retrospective Analysis for Research and Applications, Version 2 (MERRA-2). *J. Climate*, **30**, 5419–5454, https://doi.org/10.1175/JCLI- D-16-0758.1.

Glisan, J. M., W. J. Gutowski, J. J. Cassano, and M. E. Higgins, 2013: Effects of spectral nudging in WRF on Arctic temperature and precipitation simulations. *J. Climate*, **26**, 3985–3999, doi:10.1175/JCLI-D-12-00318.1.

Hall, D. K., G. A. Riggs, V. V. Salomonson, N. E. DiGirolamo and K. A. Bayr, 2002: MODIS snow-cover products. *Remote Sens. Env.*, **83**, 181-194.

Han, Y., P. van Delst, Q. Liu, F. Weng, B. Yan, R. Treadon, and J. Derber, 2006: Community Radiative Transfer Model (CRTM): Version 1, NOAA technical report, 122 pp., NOAA, Washington, D. C.

Harig, C., and Simons, F. J., 2016: Ice mass loss in Greenland, the Gulf of Alaska, and the Canadian Archipelago: Seasonal cycles and decadal trends. *Geophys. Res. Lett.*, doi:

10.1002/2016GL067759.

Hartmann, B., and G. Wendler, 2005: On the significance of the 1976 Pacific climate shift in the climatology of Alaska. *J. Climate*, **48**, 4824-4839.

Hegner H., G. Müller, V. Nespor, A. Ohmura, R. Steigrad, and H. Gilgen, 1998: World Climate Research Program WCRP (WMO/ICSU/IOC) Baseline Surface Radiation Network (BSRN): Update of the technical plan for BSRN data management, Version 1.0. Technical report 2. World Radiation Monitoring Center (WRMC), Institute of Geography ETH: Zurich, Switzerland.

Hines, K. M., and D. H. Bromwich, 2008: Development and testing of Polar Weather Research and Forecasting (WRF) Model. Part I: Greenland Ice Sheet meteorology. *Mon. Wea. Rev.*, **136**, 1971–1989, doi:10.1175/2007MWR2112.1.

——, and ——, 2017: Simulation of Late Summer Arctic Clouds during ASCOS with Polar WRF. *Mon. Wea. Rev.,* **145**, 521–541, doi: 10.1175/MWR-D-16-0079.1.

——, ——, L.-S. Bai, M. Barlage, and A. S. Slater, 2011: Development and testing of Polar Weather Research and Forecasting Model. Part III: Arctic land. *J. Climate*, **24**, 26–48, doi:10.1175/2010JCLI3460.1.

——, ——, L. Bai, C. M. Bitz, J. G. Powers, and K. W. Manning, 2015: Sea ice enhancements to Polar WRF. *Mon. Wea. Rev.*, **143**, 2363–2385, doi:10.1175/MWR-D-14-00344.1.

Huang X.-Y., and Coauthors, 2009: Four-dimensional variational data assimilation for WRF: Formulation and preliminary results. *Mon. Wea. Rev.*, **137**, 299–314.

Iacono, M. J., J. S. Delamere, E. J. Mlawer, M. W. Shepard, S. A. Clough, and W. D. Collins, 2008: Radiative forcing by long-lived greenhouse gases: Calculations with the AER radiative transfer models. *J. Geophys. Res.*, **113**, D13103, doi: 10.1029/2008JD009944.

IPCC, 2013: Climate Change 2013: The Physical Science Basis. Contribution of Working Group I to the Fifth Assessment Report of the Intergovernmental Panel on Climate Change [Stocker, T.F., D. Qin, G.-K. Plattner, M. Tignor, S.K. Allen, J. Boschung, A. Nauels, Y. Xia, V. Bex and P.M. Midgley (eds.)]. Cambridge University Press, Cambridge, United Kingdom and New York, NY, USA, 1535 pp.

Jakobson, E., T. Vihma, T. Palo, L. Jakobson, H. Keernik, and J. Jaagus, 2012: Validation of atmospheric reanalyses over the central Arctic Ocean. *Geophys. Res. Lett.*, **39**, 10, doi: 10.1029/2012GL051591.

Jiang, L., D. Tarpley, K. E. Mitchell, S. Zhou, F. N. Kogan, and W. Guo, 2008: Adjusting for long-term anomalous trends in NOAA's Global Vegetation Index data sets. *IEEE Trans. Geosc. Remote Sens.*, **46** (2), 409-422.

Jung, T., and Coauthors, 2016: Advancing polar prediction capabilities on daily to seasonal time scales. *Bull. Amer. Meteor. Soc.*, **97**, 1631–1647, doi: 10.1175/BAMS-D-14-00246.1.

Kain J. S., 2004: The Kain-Fritsch convective parameterization: An update. *J. Appl. Meteorol.*, **43**, 170 – 181.

——, and J. M. Fritsch JM, 1990: A one-dimensional entraining/detraining plume model and its application in convective parameterization. *J. Atmos. Sci.*, **47**, 2784 – 2802.

——, ——, 1993: Convective parameterization for mesoscale models: The Kain-Fritsch scheme. *The representation of cumulus convection in numerical models.* Emanuel KA, Raymond DJ. Eds. American Meteorological Society, Boston. 246 pp.

Kato, S., N. G. Loeb, F. G. Rose, D. R. Doelling, D. A. Rutan, T. E. Caldwell, L. Yu, and R. A. Weller, 2013: Surface irradiances consistent with CERES-derived top-of-atmosphere shortwave and longwave irradiances. *J. Climate*, **26**, 2719–2740, doi: 10.1175/JCLI-D-12-00436.1.

Kay, J. E., M. M. Holland, and A. Jahn, 2011: Inter-annual to multi-decadal Arctic sea ice extent trends in a warming world. *Geophys. Res. Lett.*, **38**, L15708, doi: 10.1029/2011GL048008.

Kohnemann, S. H. E., G. Heinemann, D. H. Bromwich, and O. Gutjahr, 2017: Extreme warming in the Kara Sea and Barents Sea during the winter period 2000-2016. *J. Climate*, doi: 10.1175/JCLI-D-16-0693.1, in press.

Kwok, R. and N. Untersteiner, 2011: The thinning of Arctic sea ice. *Phys. Today*, **64**(4), 36-41.

Lenaerts, J. T. M., van Angelen, J. H., van den Broeke, M. R., Gardner, A. S., Wouters, B., and van Meijgaard, E., 2013: Irreversible mass loss of Canadian Arctic Archipelago glaciers. *Geophys. Res. Lett.*, **40**, 870-874.

L'Heureux, M. L., A. Kumar, G. D. Bell, M. S. Halpert, and R. W. Higgins, 2008: Role of the Pacific-NorthAmerican (PNA) pattern in the 2007 Arctic sea ice decline. *Geophys. Res. Lett.*, **35**, L20701, doi:10.1029/2008GL035205.

Lindsay, R., M. Wensnahan, A. Schweiger, and J. Zhang, 2014: Evaluation of seven different atmospheric reanalysis products in the Arctic. *J. Climate*, **27**, 2588-2606, doi: 10.1175/JCLI-D-13-00014.1.

Liu, Z., C. S. Schwartz, C. Snyder, and S. Ha, 2012: Impact of assimilating AMSU-A radiances on forecasts of 2008 Atlantic tropical cyclones initialized with a limited-area Ensemble Kalman Filter. *Mon. Wea. Rev.*, **140**, 4017–4034.

Loeb, N. G., B. A. Wielicki, D. R. Doelling, G. Smith, D. F. Keyes, S. Kato, N. Manalo-Smith, and T. Wong, 2009: Toward optimal closure of the Earth's top-of-atmosphere radiation budget. *J. Climate*, **22**, 748–766, doi: 10.1175/2008JCLI2637.1.

Ma, Q., K. C. Wang, and M. Wild, 2015: Impact of geolocations of validation data on the evaluation of surface incident shortwave radiation from earth system models. *J. Geophys. Res. Atmos.,* **120**, 6825–6844.

Maslanik, J. A., C. Fowler, J. Stroeve, S. Drobot, J. Zwally, D. Yi, and W. Emery, 2007: A younger, thinner Arctic ice cover: Increased potential for rapid, extensive sea-ice loss. *Geophys. Res. Lett*., **34**, L24501, doi:10.1029/2007GL032043.

——, J. Stroeve, C. Fowler, and W. Emery, 2011: Distribution and trends in Arctic sea ice age through spring 2011. *Geophys. Res. Lett.*, **38**, L13502, doi:10.1029/2011GL047735.

McClelland, J. W., R. M. Holmes, B. J. Peterson, and M. Stieglitz, 2004: Increasing river discharge in the Eurasian Arctic: consideration of dams, permafrost, and fires as potential agents of change. *J. Geophys. Res.*, **109**, D18102, doi: 10.1029/2004JD004583.

Mekis, È, 2005: 'Adjustments for trace measurements in Canada'. Proceedings of the 15th Conference on Applied Climatology, 20-24 Jun 2005. Savannah, GA. American Meteorological Society: Boston, MA.

——, and W. D. Hogg, 1999: Rehabilitation and analysis of Canadian daily precipitation time series. Atmos. Ocean, **37**, 53-85.

——, and R. Hopkinson, 2004: Derivation of an improved snow water equivalent adjustment factor map for application on snowfall ruler measurements in Canada'. In Proceedings of the 14th Conference on Applied Climatology,12–15, January 2004. American Meteorological Society: Boston, MA, 12 – 15.

Moore, G. W. K., D. H. Bromwich, A. B. Wilson, I. Renfrew, and L. Bai, 2016: Arctic System Reanalysis improvements in topographically-forced winds near Greenland. *Quart. J. R. Meteorol. Soc.*, **142**, 2033-2045, doi: 10.1002/qj.2798.

Nakanishi M., 2001: Improvement of the Mellor – Yamada turbulence closure model based on large-eddy simulation data. *Bound.-Lay. Meteorol.*, **99**, 349 – 378.

——, and H. Niino, 2004: An improved Mellor – Yamada level – 3 model with condensation physics: Its design and verification. *Bound.-Lay. Meteorol.*, **112**, 1 – 31.

——, ——, 2006: An improved Mellor – Yamada level – 3 model. Its numerical stability and application to a regional prediction of advection fog. *Bound.-Lay. Meteorol.*, **119**, 397 – 407.

Nghiem, S. V., and Coauthors. 2012: The extreme melt across the Greenland ice sheet in 2012. *Geophys. Res. Lett.*, **39**, L20502, doi: 10.1029/2012GL053611016.

NSIDC, 2017: Arctic Sea Ice News and Analysis. Accessed 4/27/2017. [Available online at http://nsidc.org/arcticseaicenews/.]

Ohmura A., and Coauthors, 1998: Baseline Surface Radiation Network (BSRN/WCRP): New precision radiometry for climate research. *Bull. Am. Meteorol. Soc.*, **79**, 2115 – 2136.

Overland, J. E., and M. Wang, 2005: The Arctic climate paradox: the recent decrease of the Arctic Oscillation. *Geophys. Res. Lett.*, **32**(6), L06701, doi: 10.1029/2004GL021752.

Pan, M., and Coauthors, 2003: Snow process modeling in the North American Land Data Assimilation System (NLDAS): 2. Evaluation of model simulated snow water equivalent. *J. Geophys. Res.*, **108** (D22), 8850, doi: 10.1029/2003JD003994.

Parrish, D. F., and J. C. Derber, 1992: The National Meteorological Center's spectral statistical interpolation analysis system. *Mon. Wea. Rev.*, **120**, 1747–1763.

Peterson T. C, and D. R. Easterling, 1994: Creation of homogeneous composite climatological reference series. *Int. J. Climatol.*, **14**, 671-679.

——, and R. S. Vose, 1997: An overview of the Global Historical Climatology Network temperature database. *Bull. Am. Meteorol. Soc.*, **78**, 2837-2849.

Powers, J. G., K. W. Manning, D. H. Bromwich. J. J. Cassano, and A. M. Cayette, 2012: A decade of Antarctic science support through AMPS. *Bull. Amer. Meteor. Soc.*, **93**, 1699–1712.

——, and Coauthors, 2017: The Weather Research and Forecasting Model: Overview, system efforts, and future directions. *Bull. Amer. Meteor. Soc.*, **98,** 1717–1737, https://doi.org/10.1175/BAMS-D-15-00308.1.

Rawlins, M. A., and Coauthors, 2010: Analysis of the Arctic system for freshwater cycle intensification: Observations and expectations. *J. Climate*, **23**, 5715-5737.

Rienecker, M. M., and Coauthors, 2011: MERRA: NASA's Modern-Era Retrospective Analysis for Research and Applications. *J. Climate*, **24**, 3624–3648.

Rigor, I. G. and J. M. Wallace, 2004: Variations in the age of Arctic sea-ice and summer sea-ice extent. *Geophys. Res Letts.*, **31**, L09401, doi: 10.1029/2004GL019492.

Rignot, E., I. Velicogna, M. R. van den Broeke, A. Monaghan, and J. T. M. Lenaerts, 2011: Acceleration of the contribution of the Greenland and Antarctic ice sheets to sea level rise. *Geophys. Res. Letts.*, **38**, L05503, doi: 10.1029/2011GL046583.

Rogers, A. N., D. H. Bromwich, E. N. Sinclair, and R. I. Cullather, 2001: The atmospheric hydrologic cycle over the Arctic basin from reanalyses. Part II: Interannual variability. *J. Climate*, **14**, 2414-2429.

Romanovsky, V. E., S. L. Smith, and H. H. Christiansen, 2010: Permafrost thermal state in the polar Northern Hemisphere during the International Polar Year 2007-2009: A synthesis. *Permafrost and Periglacial Processes*, **21**, 105-116, doi: 10.1002/ppp.689.

Saha, S., and Coauthors, 2010: The NCEP Climate Forecast System Reanalysis. *Bull. Amer. Meteor. Soc.*, **91**, 1015–1057.

Samelson, R. M., and P. L. Barbour, 2008: Low-level jets, orographic effects, and extreme events in Nares Strait: A model-based mesoscale climatology. *Mon. Wea. Rev.*, **136**, 4746-4759, doi:10.1175/2007MWR2326.1.

Schaaf, C. B., and Coauthors, 2002, First operational BRDF, albedo and nadir reflectance products from MODIS. *Remote Sens. Environ.*, **83**, 135-148.

Schwartz, C. S., Z. Liu, Y. Chen, and X.-Y. Huang, 2012: Impact of assimilating microwave radiances with a limited-area ensemble data assimilation system on forecasts of Typhoon Morakot. *Wea. Forecasting*, **27**, 424–437.

Screen, J. A. and I. Simmonds, 2010: The central role of diminishing sea ice in recent Arctic temperature amplification. *Nature*, **464**, 1334-1337.

Screen J. A., C. Deser C, and I. Simmonds, 2012: Local and remote controls on observed Arctic warming. *Geophys. Res. Lett.*, **39**, L10709, doi:10.1029/2012GL051598.

Serreze, M. C., and J. Francis, 2006: The Arctic amplification debate. *Climatic Change*, **76**, doi: 10.1007/s10584-005-9017-y.

——, and A. P. Barrett, 2011: Characteristics of the Beaufort Sea High. *J. Climate*, **24**, 159-182, doi: 10.1175/2010JCLI13636.1

Skamarock, W. C., and Coauthors, 2008: A description of the Advanced Research WRF version 3. NCAR Tech. Note NCAR/TN-4751STR, 113 pp., doi:10.5065/D68S4MVH.

Slater, A. G., T. J. Bohn, J. L. McCreight, M. C. Serreze, and D. P. Lettenmaier, 2007: A multimodel simulation of pan-Arctic hydrology. *J. Geophys. Res.*, **112**, G04S45, doi:10.1029/2006JG000303.

Stöckli R., E. Vermote, N. Saleous, R. Simmon, and D. Herring, 2005: The Blue Marble Next Generation - A true color earth dataset including seasonal dynamics from MODIS. Published by the NASA Earth Observatory. Accessed 4/26/2017. [Available online at https://earthobservatory.nasa.gov/Features/BlueMarble/?src=ve].

Tao, W.-K., and J. Simpson, 1993: The Goddard Cumulus Ensemble model. Part I. Model description. *Terr. Atmos. Ocean. Sci.*, **4**, 19-54.

——, and Coauthors, 2003: Microphysics, radiation and surface processes in the Goddard Cumulus Ensemble (GCE) model. *Meteorol. Atmos. Phys*., **82**, 97 – 137.

Thompson, D. W. J., and J. M. Wallace, 2000: Annular modes in the extratropical circulation. Part I: Month-to-month variability. *J. Climate*, **13**, 1000-1016.

Tilinina N., S. K. Gulev, and D. H. Bromwich, 2014: New view of Arctic cyclone activity from the Arctic system reanalysis. *Geophys. Res. Lett.*, **41**, 1766 – 1772, doi:10.1002/2013GL058924.

Tilling, R. L., A. Ridout, A. Shepherd, and D. J. Wingham, 2015: Increased Arctic sea ice volume after anomalously low melting in 2013, *Nat. Geosci.*, **8** (8), 643-646, doi:10.1038/ngeo2489.

Walsh, J. E., F. Fetterer, J. S. Stewart, and W. L. Chapman, 2017: Database for depicting Arctic sea ice variations back to 1850. *Geographical Review*, **107** (1), 89 – 107, doi: 10.1111/j.1931-0846.2016.12195.x.

Wild, M.; D. Folini, C. Schär, N. Loeb, E. Dutton, and G. König-Langlo, 2013: The global energy balance from a surface perspective. *Clim. Dyn.*, **40**, 3107–3134.

——, ——, M. Hakuba, C. Schär, C., S. Seneviratne, S. Kato, D. Rutan, C. Ammann, E. Wood, and G. König-Langlo, 2015: The energy balance over land and oceans: An assessment based on direct observations and CMIP5 climate models. *Clim. Dyn.*, **44**, 3393–3429.

Wilson, A. B., D. H. Bromwich, and K. M. Hines, 2011: Evaluation of Polar WRF forecasts on the Arctic System Reanalysis domain: Surface and upper air analysis. *J. Geophys. Res.*, **116**, D11112, doi:10.1029/2010JD015013.

——, ——, and ——, 2012: Evaluation of Polar WRF forecasts on the Arctic System Reanalysis domain: 2. Atmospheric hydrologic cycle. *J. Geophys. Res.*, **117**, D04107, doi:10.1029/2011JD016765.

Zhang, L., A. Kumar, and W. Wang, 2012: Influence of changes in observations on precipitation: A case study for the Climate Forecast System Reanalysis (CFSR). *J. Geophys. Res.*, **117**, D8, doi: 10.1029/2011JD017347.

Zhang, X.; S. Liang, M. Wild, and B. Jiang, 2015: Analysis of surface incident shortwave radiation from four satellite products. *Remote Sens. Environ.*, **165**, 186–202.

——, ——, G. Wang, Y. Yao, B. Jiang, and J. Cheng, 2016: Evaluation of the reanalysis surface incident shortwave radiation products from NCEP, ECMWF, GSFC, and JMA using satellite and surface observations. *Remote Sensing*, **8**, 225, doi:10.3390/rs8030225.

Zheng, Y., K. Alapaty, J.A. Herwehe, A.D. Del Genio, and D. Niyogi, 2016: Improving high resolution weather forecasts using the Weather Research and Forecasting (WRF) model with an updated Kain–Fritsch scheme. *Mon. Wea. Rev.*, **144**, 833–860, doi:10.1175/MWR-D-15-0005.1.

SIDEBAR 1. ***Nares Strait Flow***. Strong low-level winds are a common cold season feature in Nares Strait located between the high terrain of Greenland and Ellesmere Island (Samelson and Barbour 2008). The strong ageostrophic winds are due to orographic channeling down the pressure gradient between high pressure over the Arctic Ocean (Lincoln Sea) and low pressure over Baffin Bay. They may play a key role in generating the persistent winter North Water polynya in northern Baffin Bay. Samelson and Barbour (2008) modeled these winds with Polar MM5 (predecessor to Polar WRF) with a resolution of 6 km. Figure SB1 shows an example one of these events that occurred on 9 February 2007 captured by the ASRv1 and ASRv2. The 15 km ASRv2 does a much better job resolving the orography of Nares Strait and thus the winds are much stronger (> 20 m s^{1}) and more continuous than at the 30 km resolution (~15 m s^{-1}) . The katabatic winds over Greenland feed into the wind flow at two locations in ASRv2. Notice the multiple centers in the low over Baffin Bay compared to the single center in ASRv1. The high over the Arctic Ocean is more clearly captured by the 15 km ASRv2. This case illustrates that topographically forced winds are much better captured by the finer resolution of ASRv2.

SIDEBAR 2. ***Kara and Barents Seas Trends.*** Figure SB2a illustrates linear trends in the spatial extent of January sea ice from 2000 to 2012. According this analysis, the strongest statistically significant trends have occurred in the Kara and Barents Seas around the island of Novaya Zemlaya (68-80°N, 60-90°E). This is consistent with the analysis by Kohnemann et al. (2017) showing that a reduction of sea ice in this region in late autumn and winter is a driver of enhanced oceanatmosphere sensible heat flux. The Novaya Zemlaya trends for this time period are approximately 40%, nearly 4 times the basin-wide sea-ice extent decline across the Arctic. Figures SB2b-e show the coupled feedback between this sea-ice loss and the atmosphere. Reduced sea ice cover enhances sensible and latent fluxes from the ocean to the atmosphere, leading to an extreme linear change in 2-m temperature over the thirteen year period of nearly 13°C (Fig. SB2b). This energy flux plays a driving role in the evaporation of moisture into the atmospheric boundary layer. Additional moisture in the atmosphere enhances downward longwave radiation at the surface, driving further increases in surface temperature and sea ice melt. Figures SB2c and SB2d support this dynamic relationship with linear changes in downward longwave radiation of 52 to 78 W m^{-2} and specific humidity between 1.04 and 2.08 g kg^{-1} for 2000-2012, all statistically significant with p-values < 0.01. Additionally, the increased moisture leads to significant positive cloud and precipitation trends downwind (and consistent with the mean flow) from the strongest sea-ice decline east of Novaya Zemlaya (Fig. SB2e). Together, these results demonstrate the capacity to use ASRv2 in a detailed analysis of atmospheric processes associated with surface changes in the Arctic.

TABLES

Table 1: ASRv2 production system at-a-glance

Model	**Polar WRF 3.6.0***
Dynamical Core	Fully Compressible, Euler Non-hydrostatic
Time-stepping Scheme	Time-split integration using a 3rd-order Runge-Kutta scheme
Vertical Coordinate	Terrain-following, Dry Hydrostatic-Pressure
Horizontal Resolution & Grid	15 km* / Arakawa C-grid staggered
Vertical Resolution and Model Top	71 vertical levels; First level at 4 m; 25 levels below 850 hPa; 10 hPa top
Lateral Boundary Conditions	ERAI surface/upper-level model data; Spectrally nudged above 100 hPa*
Physics Parameterizations	
Microphysics	Goddard
Cumulus	Kain-Fritsch (with sub-grid cloud fraction interaction with radiation*)
Radiation (Short and Longwave)	Rapid Radiative Transfer Model (RRTMG)
Planetary Boundary Layer and Surface Layer	Mellor-Yamada-Nakanishi-Niino 2.5 (MYNN)
Data Assimilation	**WRFDA 3.3.1 (3D-Var)**
Method	Dual outer loop*; 3-hr cycle; Assimilate observations within ±1.5 of analysis
Background Error	Computed for every month based on 12h & 24h Polar WRF forecasts
Data	
Conventional Data	NCEP PREPBUFR
Sea surface winds	QuickSCAT and SSM/I
Satellite radiances	AMSUA, AMSUB, AIRS, MHS, HIRS3, and HIRS4
GPS	RO and IPW
Land Surface Model	**NOAH LSM with HRLDAS**
Snow cover: depth and density	NCEP Final Analysis
Land-surface albedo	MODIS updated every 8 days / Greenland - updated daily
Orography	USGS GTOPO 2' / Greenland - 1 km DEM (Bamber *et al*., 2001)
Vegetation	MODIS - updated every 8 days
Soil	Initialized with ERAI soil temperature and moisture
Ocean Conditions	**Prescribed (based on reanalysis and observations)**
SST	ERAI
Sea-ice	
Concentration & Thickness	AMSRE 6.25 km (summer 2002-2011); Alternative 25 km satellite based products (2000-summer 2002, 2012) [See Masanlik et al. 2007, 2011]
Albedo	Annually varying seasonal cycle based on melt/freeze date observations from satellite passive microwave measurements
Snow Cover on Sea-Ice	Seasonally Varying

***Changes since ASRv1 – see text for details.**

Table 2: Long-term monthly and annual mean bias, RMSE, and correlation for ERAI, ASRv1, and ASRv2 for 2000-2010.

Month	10-m Wind Speed (m s^{-1}) Bias			RMSE			Correlation		
	ERAI	ASRv1	ASRv2	ERAI	ASRv1	ASRv2	ERAI	ASRv1	ASRv2
January	0.70	-0.06	0.39	2.36	1.92	1.55	0.67	0.71	0.80
February	0.57	-0.08	0.38	2.27	1.90	1.56	0.67	0.71	0.80
March	0.40	-0.19	0.27	2.22	1.89	1.50	0.67	0.73	0.82
April	0.21	-0.31	0.20	2.11	1.82	1.48	0.65	0.72	0.81
May	0.18	-0.35	0.19	2.04	1.77	1.38	0.62	0.69	0.81
June	0.20	-0.29	0.21	1.97	1.70	1.33	0.60	0.67	0.79
July	0.25	-0.27	0.23	1.93	1.65	1.30	0.58	0.65	0.78
August	0.30	-0.22	0.25	1.92	1.63	1.28	0.59	0.65	0.78
September	0.46	-0.17	0.29	2.03	1.68	1.36	0.63	0.69	0.79
October	0.54	-0.16	0.28	2.15	1.75	1.41	0.66	0.71	0.80
November	0.59	-0.15	0.34	2.26	1.84	1.47	0.66	0.71	0.81
December	0.66	-0.10	0.36	2.34	1.92	1.53	0.66	0.70	0.80
Grand Mean	0.42	-0.19	0.28	2.13	1.79	1.43	0.64	0.69	0.80

Month	2-m Temperature (°C) Bias			RMSE			Correlation		
	ERAI	ASRv1	ASRv2	ERAI	ASRv1	ASRv2	ERAI	ASRv1	ASRv2
January	0.37	0.15	-0.01	2.15	1.52	1.24	0.92	0.96	0.97
February	0.34	0.07	-0.06	2.13	1.42	1.22	0.92	0.96	0.97
March	0.28	0.05	-0.11	2.04	1.33	1.08	0.93	0.96	0.97
April	0.24	0.08	-0.04	1.99	1.26	0.96	0.92	0.96	0.97
May	0.22	0.06	-0.07	1.99	1.27	1.08	0.92	0.96	0.97
June	0.23	0.06	-0.08	1.97	1.36	1.08	0.91	0.95	0.97
July	0.26	0.03	-0.11	1.94	1.30	1.07	0.90	0.95	0.96
August	0.27	0.06	-0.08	1.89	1.27	1.04	0.90	0.95	0.97
September	0.27	0.10	-0.05	1.86	1.25	1.05	0.92	0.96	0.97
October	0.30	0.15	-0.01	1.84	1.25	1.05	0.92	0.96	0.97
November	0.36	0.25	0.04	1.93	1.43	1.07	0.92	0.96	0.97
December	0.40	0.25	0.07	2.09	1.53	1.18	0.92	0.96	0.97

Grand Mean	0.29	0.11	-0.04	1.98	1.35	1.09	0.92	0.96	0.97

Table 2 cont.

Month	**Bias**			**2-m Dew Point Temperature (°C)** **RMSE**			**Correlation**		
	ERAI	**ASRv1**	**ASRv2**	**ERAI**	**ASRv1**	**ASRv2**	**ERAI**	**ASRv1**	**ASRv2**
January	0.61	0.19	0.00	2.34	2.06	1.86	0.92	0.94	0.95
February	0.56	0.05	0.11	2.33	1.98	1.88	0.91	0.94	0.94
March	0.45	0.01	0.09	2.30	1.86	1.68	0.91	0.94	0.95
April	0.32	-0.03	0.09	2.24	1.78	1.47	0.88	0.93	0.95
May	0.11	-0.19	0.11	2.12	1.70	1.50	0.87	0.92	0.93
June	-0.12	-0.38	0.17	2.00	1.74	1.46	0.85	0.90	0.92
July	-0.22	-0.05	0.27	1.90	1.59	1.42	0.82	0.88	0.91
August	-0.17	-0.20	0.23	1.86	1.58	1.39	0.84	0.89	0.92
September	-0.03	-0.28	0.13	1.85	1.60	1.42	0.89	0.92	0.94
October	0.12	-0.04	0.07	1.87	1.58	1.43	0.91	0.94	0.95
November	0.33	0.07	0.00	2.02	1.79	1.47	0.92	0.94	0.96
December	0.55	0.17	-0.04	2.26	2.00	1.66	0.92	0.94	0.95
Grand Mean	0.21	-0.06	0.10	2.09	1.77	1.55	0.89	0.92	0.94

Month	**Bias**			**Surface Pressure (hPa)** **RMSE**			**Correlation**		
	ERAI	**ASRv1**	**ASRv2**	**ERAI**	**ASRv1**	**ASRv2**	**ERAI**	**ASRv1**	**ASRv2**
January	0.11	0.05	0.05	1.06	0.91	0.80	0.99	0.99	0.99
February	0.11	0.06	0.01	1.01	0.88	0.80	0.99	0.99	0.99
March	0.04	0.06	0.01	0.98	0.86	0.76	0.99	0.99	0.99
April	-0.02	0.01	-0.05	0.92	0.83	0.71	0.99	0.99	0.99
May	-0.08	0.00	-0.10	0.89	0.80	0.70	0.99	0.99	0.99
June	-0.14	0.01	-0.11	0.88	0.79	0.68	0.98	0.99	0.99
July	-0.18	0.01	-0.11	0.87	0.76	0.67	0.98	0.98	0.98
August	-0.15	0.01	-0.09	0.86	0.76	0.66	0.98	0.98	0.99
September	-0.06	0.02	-0.05	0.90	0.81	0.71	0.98	0.99	0.99
October	0.01	0.03	-0.07	0.91	0.81	0.75	0.99	0.99	0.99
November	0.07	0.05	0.02	0.96	0.85	0.74	0.99	0.99	0.99
December	0.11	0.06	0.05	1.03	0.90	0.78	0.99	0.99	0.99

Grand Mean	-0.01	0.03	-0.04	0.94	0.83	0.73	0.99	0.99	0.99

Table 3: Forecast downward shortwave and longwave radiation at the surface compared to ground-stations for December 2006 - November 2007

Mid-latitude Stations	**Shortwave**								
Month (# of stations)	**Bias (W m^{-2})**			**RMSE (W m^{-2})**			**Correlation**		
	ERA	**ASRv1**	**ASRv2**	**ERA**	**ASRv1**	**ASRv2**	**ERA**	**ASRv1**	**ASRv2**
DEC (5)	4.5	19.6	16.4	61.9	53.4	47.1	0.76	0.90	0.91
JAN (5)	1.6	17.9	13.3	70.3	47.4	43.7	0.79	0.95	0.94
FEB (5)	6.4	26.9	19.7	94.2	68.6	65.5	0.81	0.93	0.92
MAR (5)	21.8	43.8	30.0	130.4	110.5	96.7	0.83	0.92	0.93
APR (5)	14.5	45.3	36.1	146.9	109.9	98.0	0.87	0.95	0.96
MAY (5)	20.1	61.5	34.5	152.5	145.9	132.5	0.86	0.92	0.92
JUN (5)	18.0	70.5	38.5	162.8	158.7	145.5	0.85	0.91	0.90
JUL (5)	31.0	70.7	42.7	159.9	156.5	153.4	0.84	0.90	0.87
AUG (5)	22.7	55.8	35.3	145.1	131.5	122.6	0.86	0.92	0.92
SEP (5)	16.3	36.2	20.0	131.2	111.8	101.9	0.84	0.91	0.91
OCT (5)	11.8	31.7	20.1	99.7	90.3	76.0	0.84	0.91	0.93
NOV (5)	[redacted]	23.5	17.8	[redacted]	70.2	60.5	0.78	0.88	0.90
Annual		**42.0**	**27.0**		**104.6**	**95.3**	**0.83**	**0.92**	**0.92**

Mid-latitude Stations	**Longwave**								
Month (# of stations)	**Bias (W m^{-2})**			**RMSE (W m^{-2})**			**Correlation**		
	ERA	**ASRv1**	**ASRv2**	**ERA**	**ASRv1**	**ASRv2**	**ERA**	**ASRv1**	**ASRv2**
DEC (5)	-9.1	-14.2	-11.9	27.9	32.2	31.0	0.75	0.72	0.73
JAN (5)	-6.5	-12.5	-6.6	25.1	30.0	26.9	0.79	0.78	0.80
FEB (5)	-8.0	-11.0	-6.5	25.4	29.5	27.1	0.82	0.76	0.79
MAR (5)	-10.5	-13.3	-7.4	26.3	28.5	27.1	0.79	0.77	0.79
APR (5)	-10.9	-12.0	-9.5	22.1	24.5	22.5	0.84	0.80	0.83
MAY (5)	-9.9	-10.7	-5.8	21.5	23.1	22.3	0.84	0.83	0.82
JUN (5)	-10.3	-12.4	-6.2	23.2	24.7	23.4	0.76	0.75	0.73
JUL (5)	-10.1	-10.8	-6.0	21.2	21.8	21.0	0.81	0.77	0.75
AUG (5)	-8.9	-9.1	-4.2	20.7	22.6	21.2	0.73	0.72	0.75

SEP (5)	-8.9	-8.8	-4.0	20.8	24.2	23.3	0.82	0.76	0.77
OCT (4)	-5.9	-8.9	-5.7	22.2	25.1	24.3	0.81	0.78	0.78
NOV (5)	-7.1	-12.7	-7.9	[redacted]	29.6	28.3	0.80	0.76	0.78
Annual	**-8.8**	**-11.4**	**-6.8**		**26.3**	**24.9**	**0.80**	**0.77**	**0.78**

Table 3 cont.

Polar Stations	**Shortwave**								
Month (# of stations)	**Bias (W m^{-2})**			**RMSE (W m^{-2})**			**Correlation**		
	ERA	**ASRv1**	**ASRv2**	**ERA**	**ASRv1**	**ASRv2**	**ERA**	**ASRv1**	**ASRv2**
DEC (0)									
JAN (4)	-1.1	-0.7	-0.9	2.7	2.1	2.5	0.67	0.69	0.67
FEB (6)	-4.2	1.7	1.7	19.7	13.1	13.9	0.79	0.88	0.87
MAR (6)	-10.0	5.8	9.1	51.9	30.7	35.4	0.86	0.94	0.94
APR (6)	-18.3	18.2	20.2	77.2	57.9	62.7	0.89	0.95	0.94
MAY (6)	-1.4	46.7	37.6	93.3	91.8	94.7	0.89	0.92	0.90
JUN (6)	-8.7	37.2	25.5	103.3	111.9	107.4	0.87	0.88	0.88
JUL (6)	-12.3	34.5	34.5	101.1	117.5	116.0	0.85	0.85	0.85
AUG (5)	-9.7	33.0	23.7	77.9	88.5	98.0	0.86	0.87	0.84
SEP (5)	-5.1	16.3	10.9	56.0	54.6	53.9	0.83	0.89	0.88
OCT (5)	-2.2	1.4	0.8	23.3	20.3	21.1	0.79	0.86	0.86
NOV (4)	[redacted]	-0.5	-0.8	[redacted]	3.6	4.0	0.76	0.87	0.86
Annual		**17.6**	**14.8**		**53.8**	**55.4**	**0.82**	**0.87**	**0.86**

Polar Stations	**Longwave**								
Month (# of stations)	**Bias (W m^{-2})**			**RMSE (W m^{-2})**			**Correlation**		
	ERA	**ASRv1**	**ASRv2**	**ERA**	**ASRv1**	**ASRv2**	**ERA**	**ASRv1**	**ASRv2**
DEC (4)	-10.6	-12.5	-20.5	30.7	36.6	37.9	0.74	0.70	0.71
JAN (4)	-9.6	-8.0	-13.5	31.3	33.4	31.8	0.73	0.69	0.73
FEB (4)	-14.6	-9.7	-14.0	33.2	29.8	30.7	0.72	0.75	0.77
MAR (3)	-6.7	-7.3	-9.1	24.4	26.6	26.9	0.81	0.76	0.72
APR (3)	-0.4	-17.4	-16.4	26.7	35.7	33.7	0.72	0.71	0.73
MAY (3)	-11.3	-23.6	-20.5	29.9	41.3	40.3	0.60	0.54	0.55
JUN (3)	2.9	-6.5	-5.7	28.2	35.3	29.6	0.52	0.40	0.51

JUL (3)	0.9	-11.3	-15.4	26.7	33.3	34.1	0.45	0.43	0.37
AUG (2)	2.5	-14.1	-18.7	23.4	32.2	36.5	0.60	0.55	0.54
SEP (2)	-9.7	-16.2	-9.3	27.7	37.0	32.1	0.61	0.48	0.51
OCT (2)	-3.5	0.8	-0.8	24.6	30.9	44.9	0.66	0.47	0.58
NOV (2)	[redacted]	-15.9	-22.6	[redacted]	35.9	37.0	0.70	0.60	0.65
Annual		**-11.8**	**-13.9**		**34.0**	**34.6**	**0.66**	**0.59**	**0.61**

FIGURE CAPTIONS

Figure 1. Topographic relief map based on Bluemarble imaging (Stöckli et al., 2005) showing inner domain of ASRv2. River shapefiles produced by Natural Earth (naturalearthdata.com) and sea-ice shapefiles produced by NSIDC (nsidc.org) showing maximum extent (white shading) in March 2012 and minimum extent (black line) in September 2012.

Figure 2. Snapshot coverage of non-radiance observations over the ASR domain within □1.5-hour time window centered at 0000 UTC on the January 1, 2007 including synoptic surface observations (black dots), metar airport observations (purple pluses), ship observations (royal blue dots), buoys (navy blue dots), radiosondes (purple asterisks), global positioning system refractivity observations (red dots), wind profiler (yellow dots), aviation in-flight weather report (green dots), QuikScat sea-surface winds (orange dots), and satellite atmospheric motion vectors (aqua dots).

Figure 3. Time series over a period of 13 years (2000-2012) of global statistics of bias (left panels) and standard deviation (right panels) of observed minus CRTM-calculated brightness temperatures with ERAI reanalyses as input, for AMSU-A channels 5~9 from 6 satellites. The dates marked in the left panels are the starting dates from which the corresponding radiance data began available.

Right panels also list important blacklist of radiance channels (see text).

Figure 4. Example grid point ASRv2 time-varying snow-covered maximum albedo (blue dots; top panel) and snow-free minimum albedo (red dots; top panel) generated from the MODIS albedo product (black solid line; top panel) and MODIS snow cover products (bottom panel). Example time series are shown for 2007 over a north Alaska grid point (68.8°N, 154.9°W).

Figure 5. Annual mean biases for the period 2000-2010 for the ASRv2 (left) and ERAI (right) for (a,b) 10-m wind speed (m s^{-1}) and (c,d) 2-m temperature (°C). Magnitudes of the biases are given by the color scale and the size of the symbol.

Figure 6. (a) ASRv2 mean 500 hPa temperature (°C), (b) difference (°C) between ASRv2 and ERAI for 500 hPa temperature, (c) ASRv2 mean 700 hPa relative humidity (%), and (d) difference (%) between ASRv2 and ERAI for 700 hPa relative humidity for the period December 2006 – November 2007. Areas where the 700 hPa pressure level exists below ground based on the annual average surface pressure have been masked in gray.

Figure 7. (a) ASRv2 mean annual total precipitation (x 10^2 mm) and (b) difference (%) between ASRv2 and ERAI for the period 2000-2010. Black dots in Fig. 7a represent station gauges used for (c) mid-latitude and (d) polar comparison of monthly precipitation bias (%) for December 2006 – November 2007.

Figure 8. Bias (W m^{-2}) of annual mean downward shortwave (top) and longwave (bottom) radiation at the surface for ASRv2 (left) and ERAI (right) compared to CERES-EBAF satellite product for December 2006 – November 2007..

Figure 9. Streamlines and wind speeds (colors) at 10-m for an intense orographically channeled wind event in Nares Strait on 9 February 2007 as captured by a) ASRv1 and b) ASRv2.

Figure 10. Linear trends between 2000-2012 in ASRv2 (a) January sea-ice fraction (b) 2-m temperature (°C yr^{-1}), (c) downward surface longwave radiation at the surface (W m^{-2} yr^{-1}), (c) 2m specific humidity (g kg^{-1} yr^{-1}), and (e) precipitation (% yr^{-1}). Unidirectional hatch marks indicate a p-value less than 0.05 and cross-hatch marks indicate p-values less than 0.01.

Figure SB1. Streamlines and wind speeds (colors) at 10-m for an intense orographically channeled wind event in Nares Strait on 9 February 2007 as captured by a) ASRv1 and b) ASRv2.

Figure SB2. Linear January trends between 2000-2012 in ASRv2 for (a) sea-ice fraction (b) 2-m temperature (°C yr^{-1}), (c) downward surface longwave radiation at the surface (W m^{-2} yr^{-1}), (c) 2m specific humidity (g kg^{-1} yr^{-1}), and (e) precipitation (% yr^{-1}). Unidirectional hatch marks indicate a p-value less than 0.05 and cross-hatch marks indicate p-values less than 0.01.

FIGURES

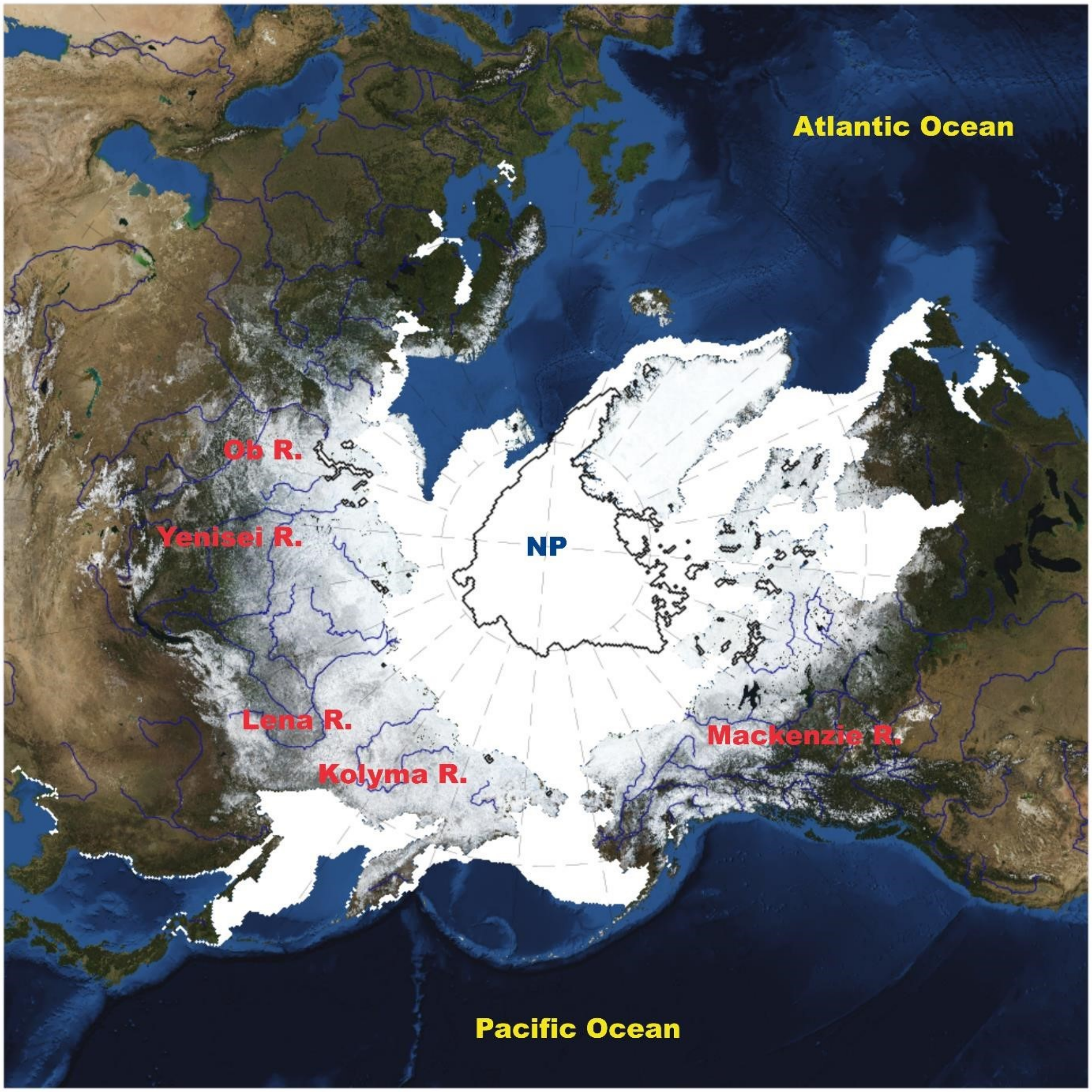

Figure 1. Topographic relief map based on Bluemarble imaging (Stöckli et al. 2005) showing inner domain of ASRv2. River shapefiles produced by Natural Earth (naturalearthdata.com) and sea-ice shapefiles produced by NSIDC (nsidc.org) showing maximum extent (white shading) in March 2012 and minimum extent (black line) in September 2012.

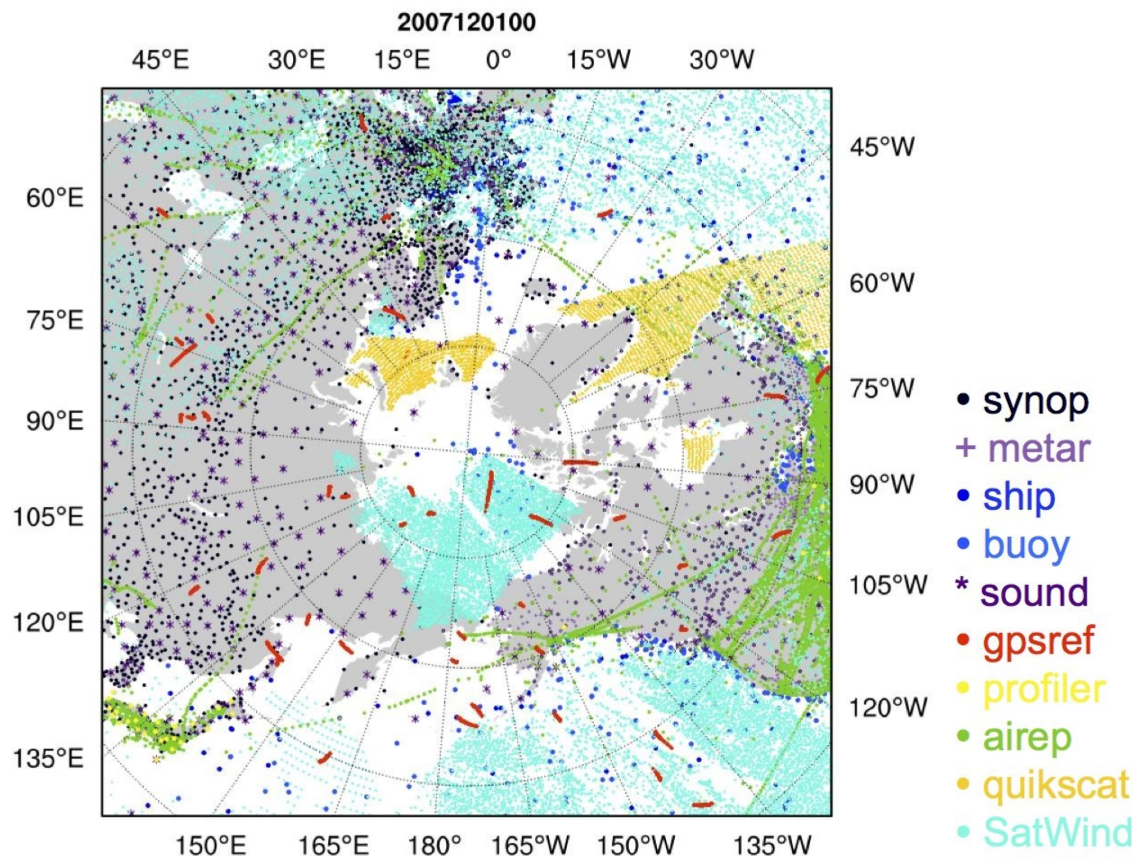

Figure 2. Snapshot coverage of non-radiance observations over the ASR domain within ±1.5-hour time window centered at 0000 UTC on the January 1, 2007 including synoptic surface observations (black dots), metar airport observations (purple pluses), ship observations (royal blue dots), buoys (navy blue dots), radiosondes (purple asterisks), global positioning system refractivity observations (red dots), wind profiler (yellow dots), aviation in-flight weather report (green dots), QuikScat sea-surface winds (orange dots), and satellite atmospheric motion vectors (aqua dots).

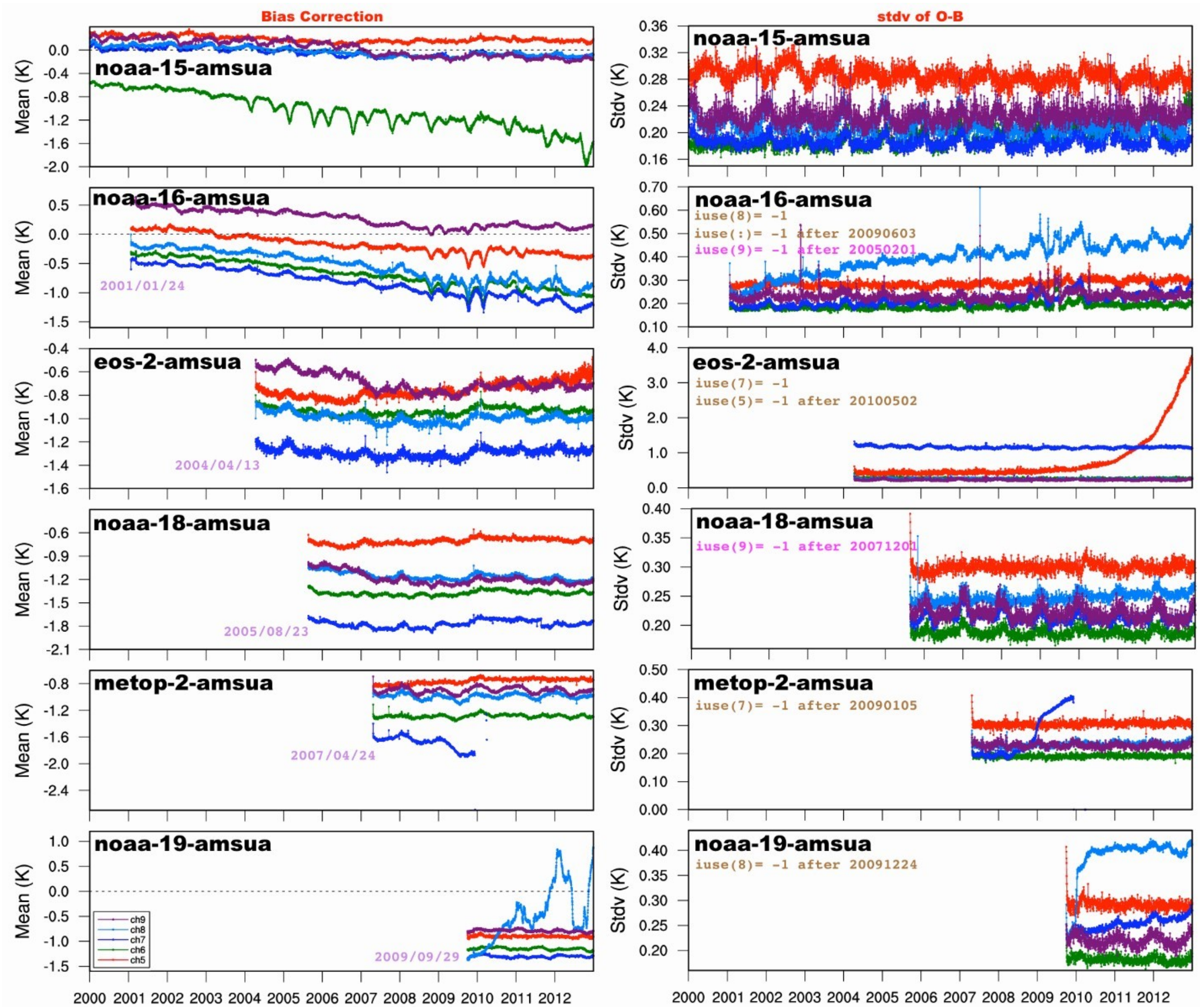

Figure 3. Time series over a period of 13 years (2000-2012) of global statistics of bias (left panels) and standard deviation (right panels) of observed minus CRTM-calculated brightness temperatures with ERAI reanalyses as input, for AMSU-A channels 5~9 from 6 satellites. The dates marked in the left panels are the starting dates from which the corresponding radiance data began available. Right panels also list important blacklist of radiance channels (see text).

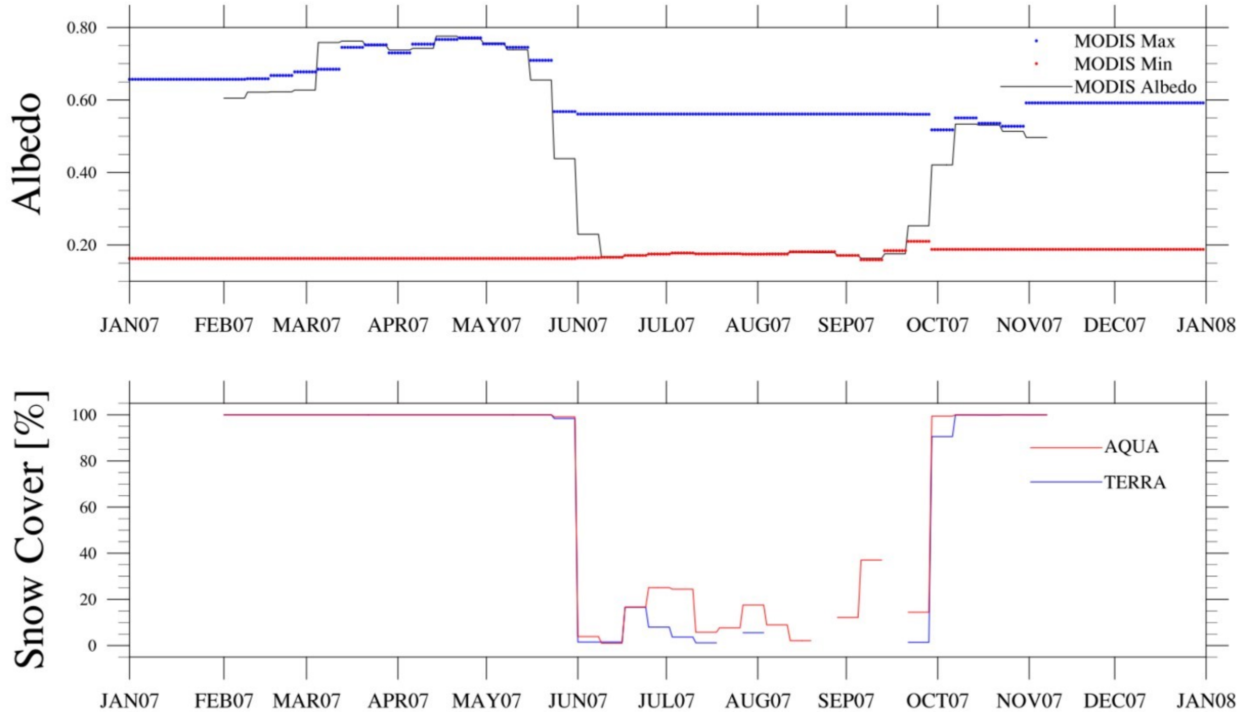

Figure 4. Example grid point ASRv2 time-varying snow-covered maximum albedo (blue dots; top panel) and snow-free minimum albedo (red dots; top panel) generated from the MODIS albedo product (black solid line; top panel) and MODIS snow cover products (bottom panel). Example time series are shown for 2007 over a north Alaska grid point (68.8°N, 154.9°W).

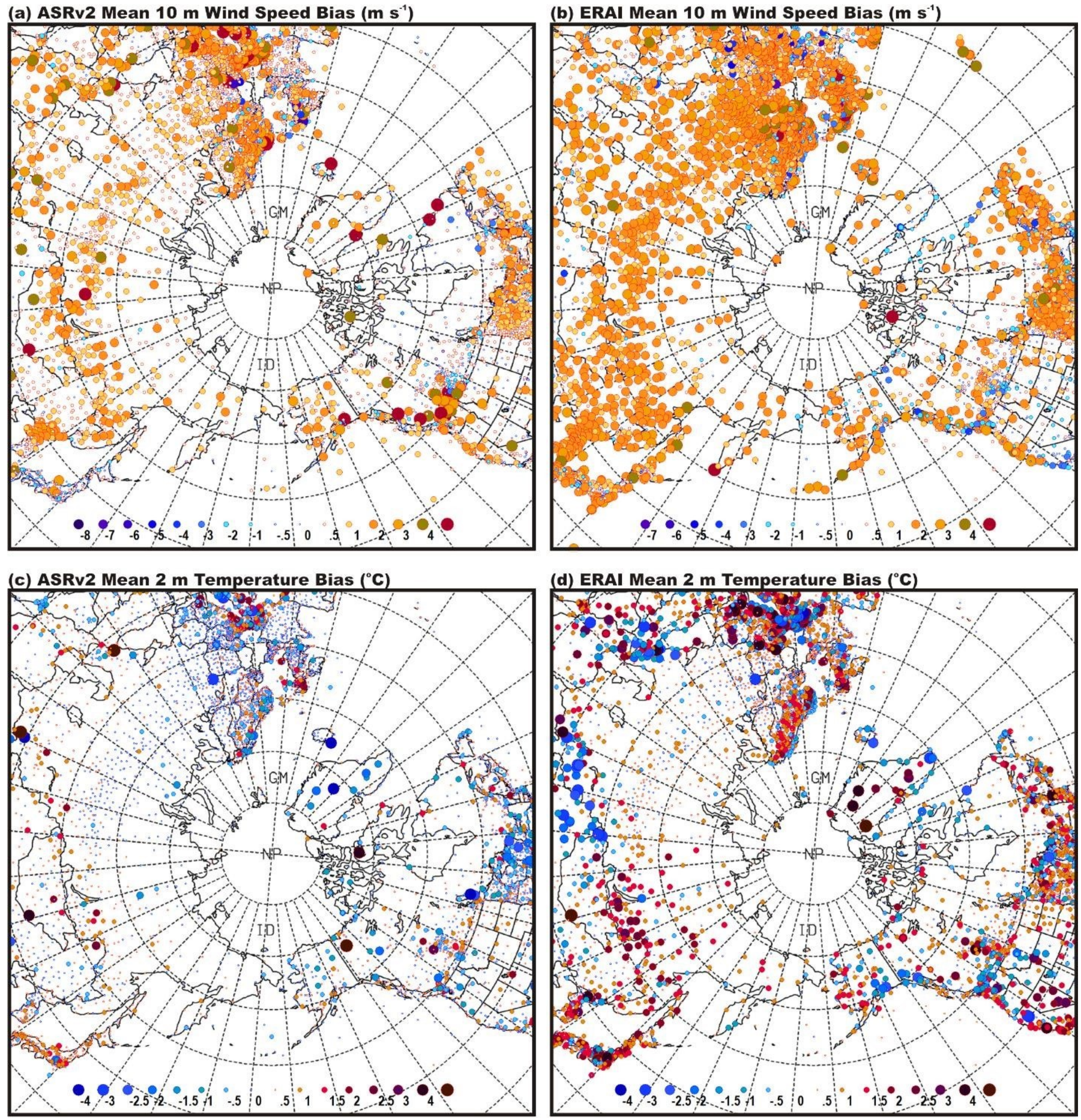

Figure 5. Annual mean biases for the period 2000-2010 for the ASRv2 (left) and ERAI (right) for (a,b) 10-m wind speed (m s^{-1}) and (c,d) 2-m temperature (°C). Magnitudes of the biases are given by the color scale and the size of the symbol.

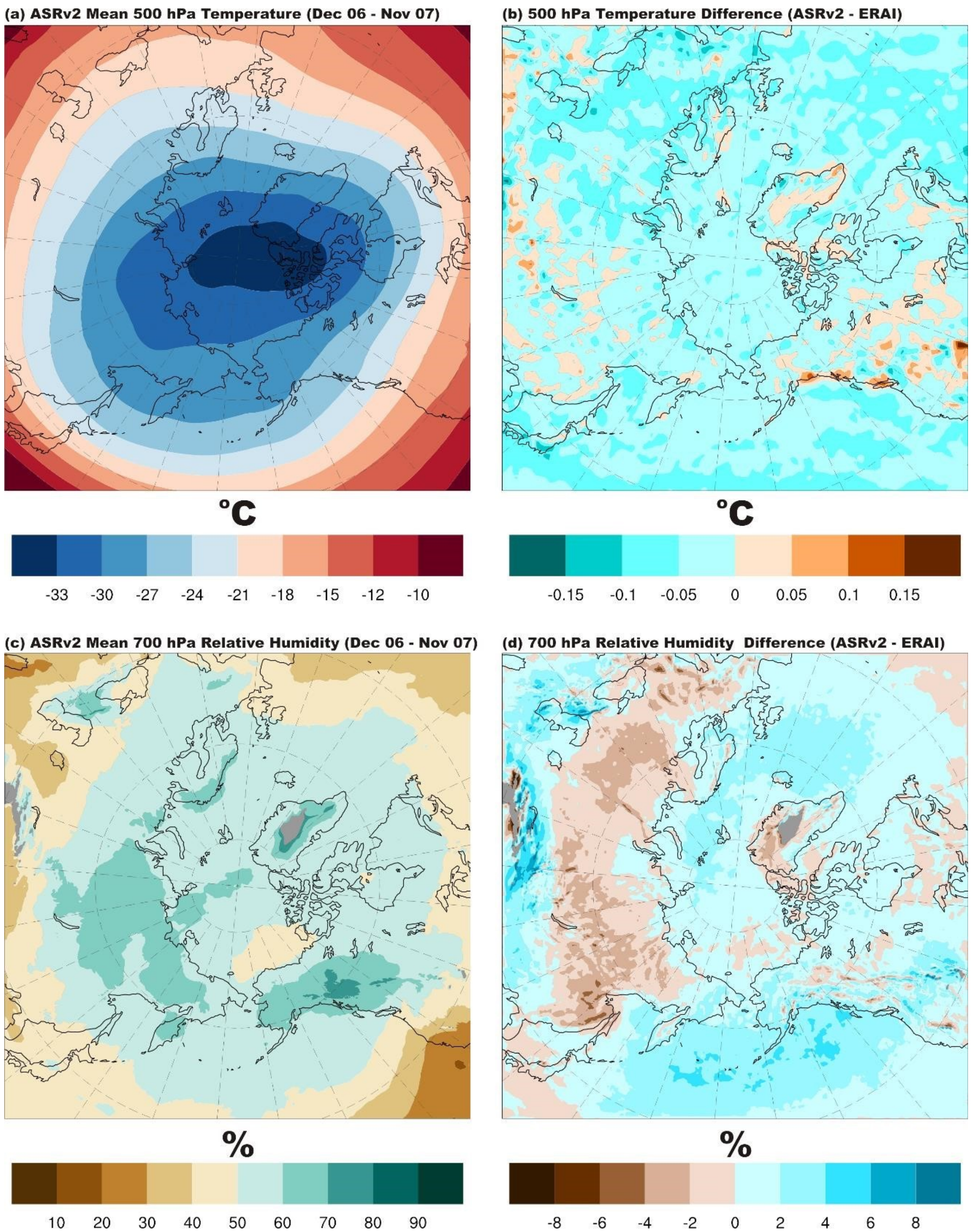

Figure 6. (a) ASRv2 mean 500 hPa temperature (°C), (b) difference (°C) between ASRv2 and ERAI for 500 hPa temperature, (c) ASRv2 mean 700 hPa relative humidity (%), and (d) difference (%) between ASRv2 and ERAI for 700 hPa relative humidity for the period December 2006 – November 2007. Areas where the 700 hPa pressure level exists below ground based on the annual average surface pressure have been masked in gray.

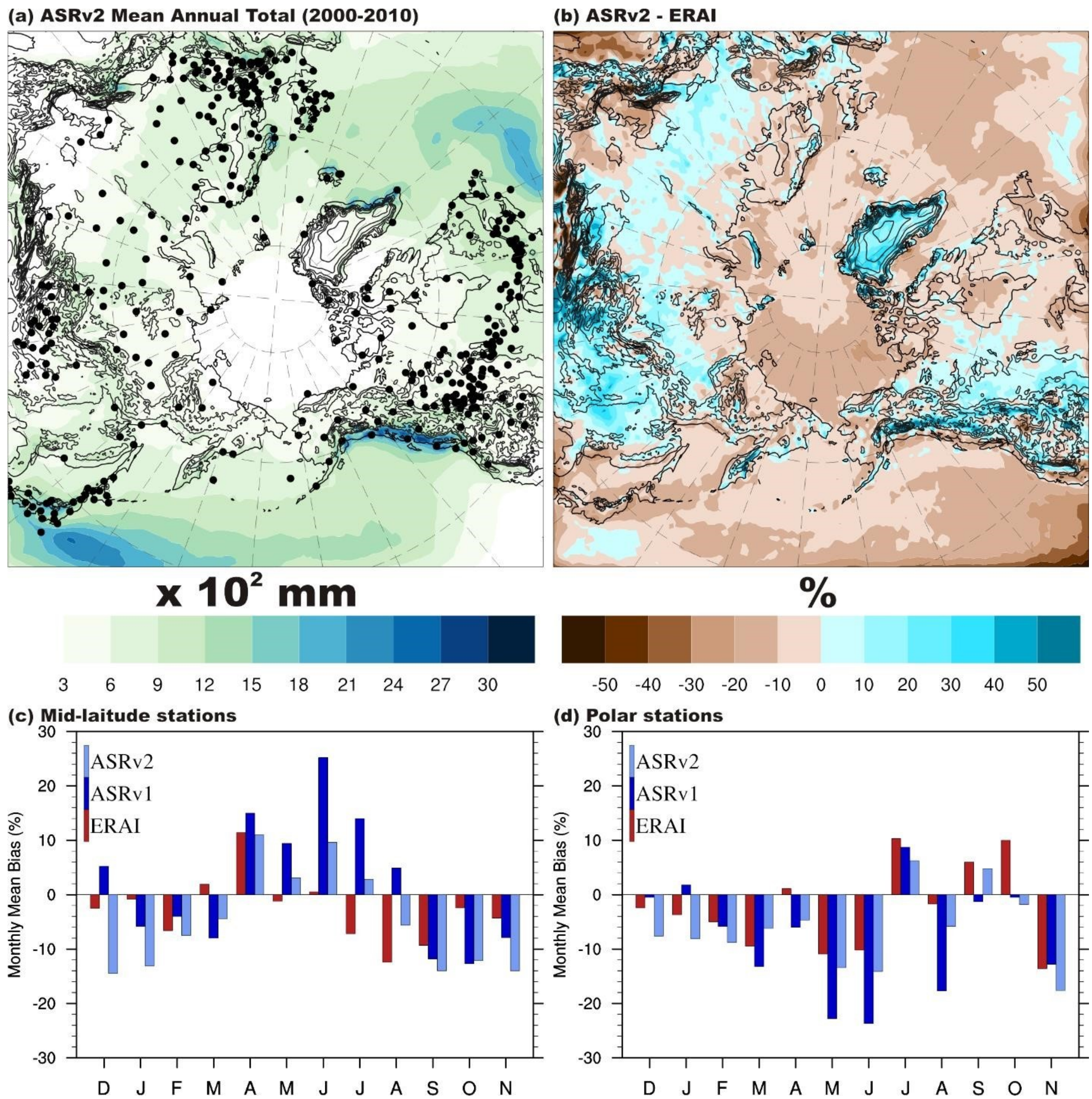

Figure 7. (a) ASRv2 mean annual total precipitation (x 10^2 mm) and (b) difference (%) between ASRv2 and ERAI for the period 2000-2010. Black dots in Fig. 7a represent station gauges used for (c) mid-latitude and (d) polar comparison of monthly precipitation bias (%) for December 2006 – November 2007.

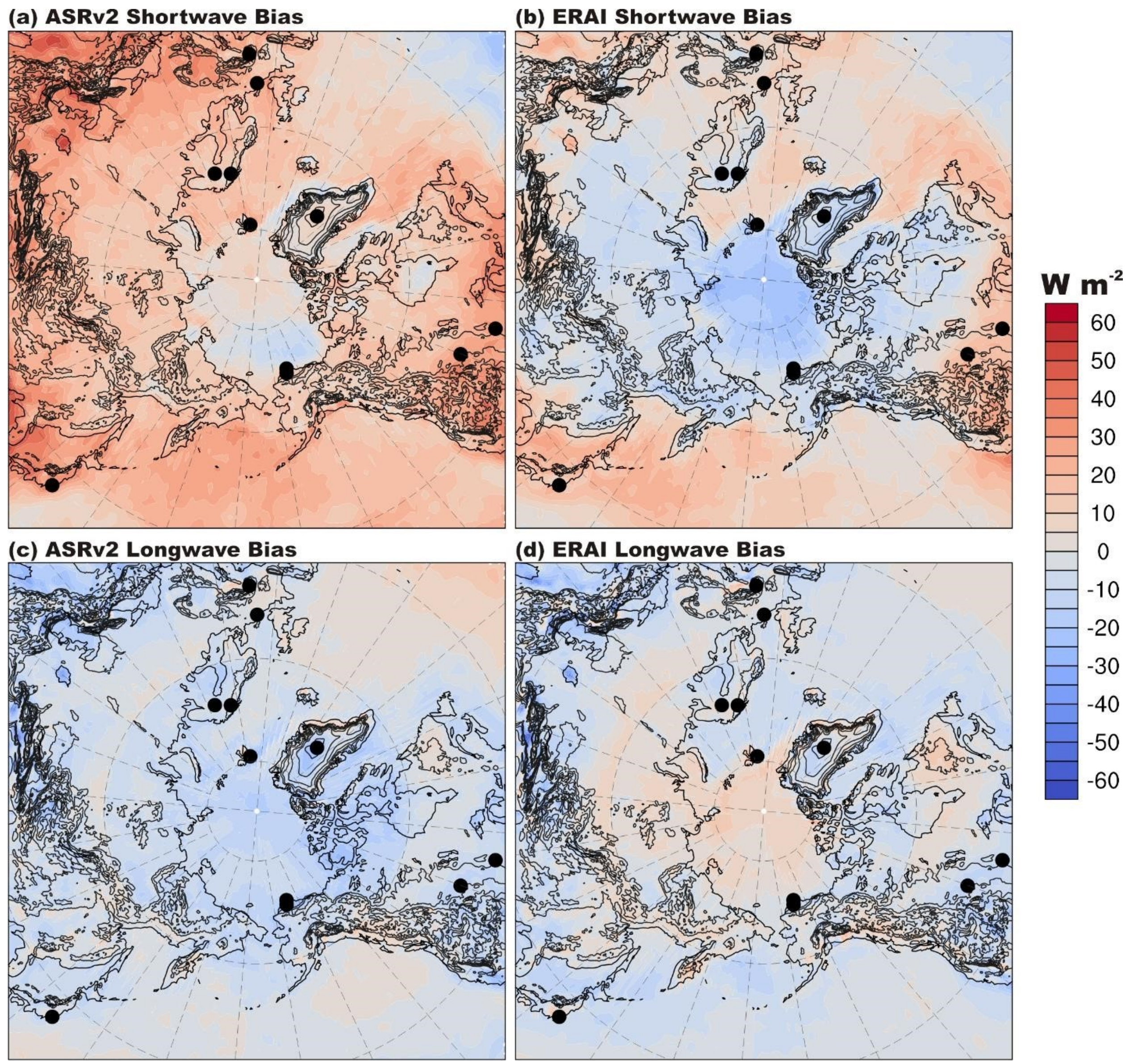

Figure 8. Bias (W m^{-2}) of annual mean downward shortwave (top) and longwave (bottom) radiation at the surface for ASRv2 (left) and ERAI (right) compared to CERES-EBAF satellite product for December 2006 – November 2007.

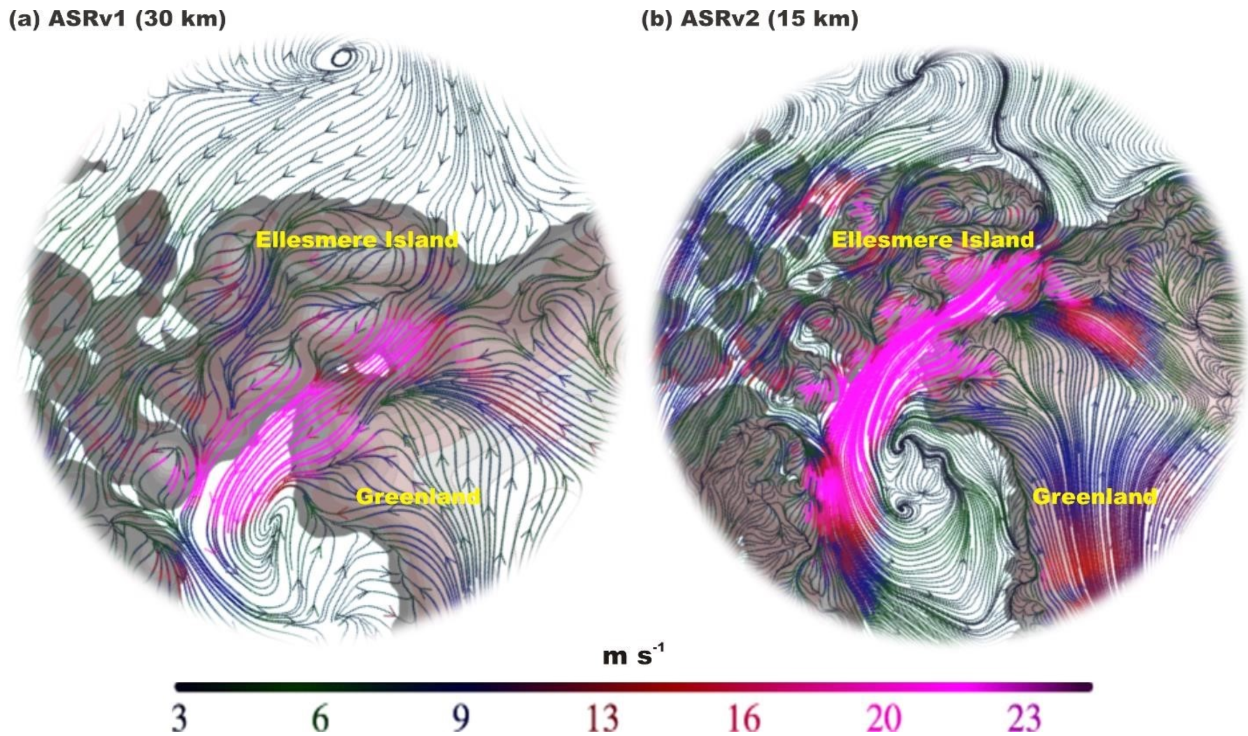

Figure SB1. Streamlines and wind speeds (colors) at 10-m for an intense orographically channeled wind event in Nares Strait on 9 February 2007 as captured by a) ASRv1 and b) ASRv2.

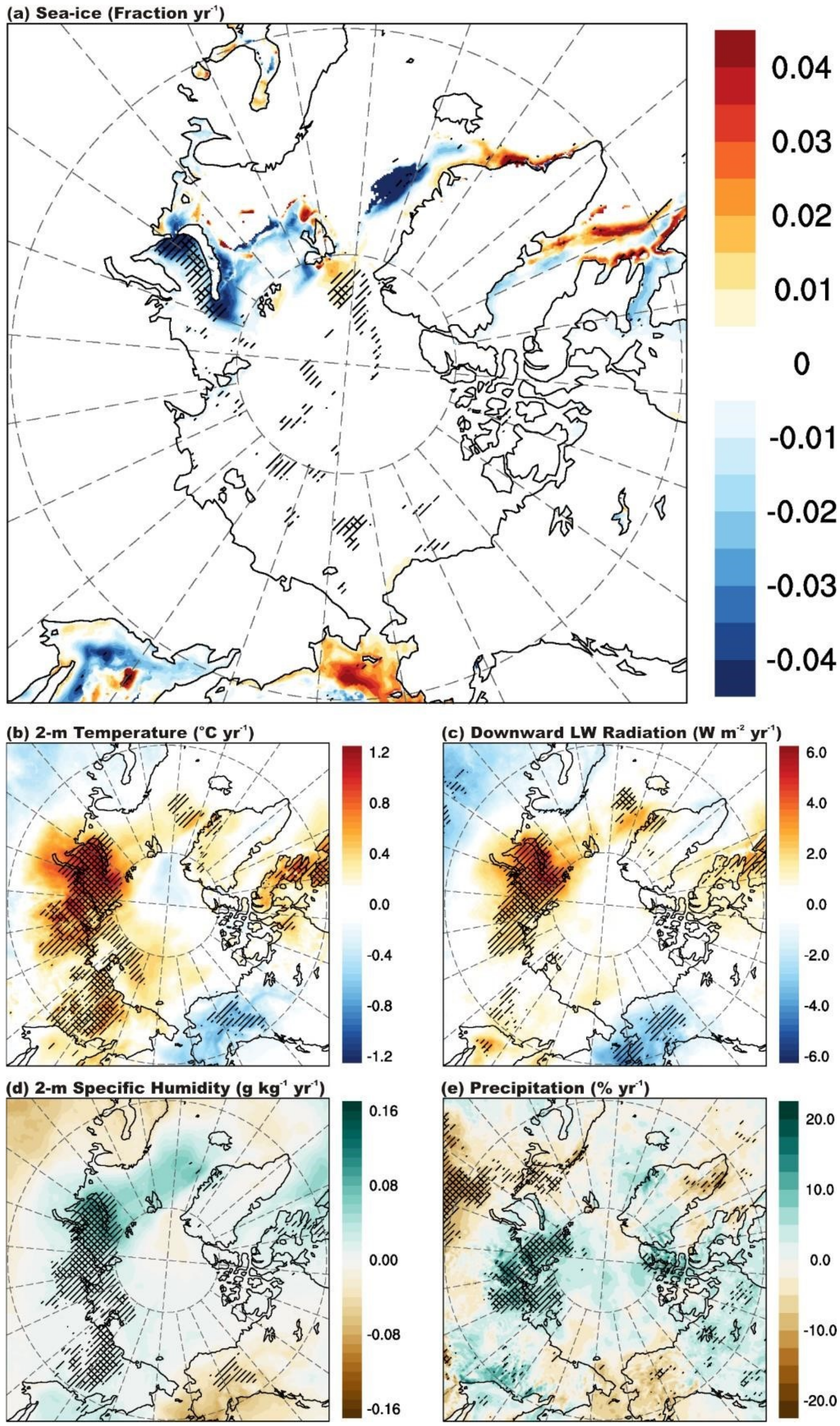

Figure SB2. Linear January trends between 2000-2012 in ASRv2 for (a) sea-ice fraction (b) 2-m temperature (°C yr^{-1}), (c) downward surface longwave radiation at the surface (W m^{-2} yr^{-1}), (c) 2m specific humidity (g kg^{-1} yr^{-1}), and (e) precipitation (% yr^{-1}). Unidirectional hatch marks indicate a p-value less than 0.05 and cross-hatch marks indicate p-values less than 0.01.